Review of wavenumber frequency spectrum models of TBL wall pressure fluctuations in 2D/1D forms

Kun Zhao [a,*] , Yimeng Li[a,b], Rui Pei [c], Hongzhou Li[b], Gareth J. Bennett[d]

Kun Zhao,[*] and Yimeng Li.[†]
Key Lab of Aerodynamic Noise Control, China Aerodynamics Research and Development Center, Mianyang, Sichuan 621000, China

Rui Pei [‡]
School of Information Science and Engineering, Shenyang University of Technology, Shenyang, 110870, China

Hongzhou Li[§]
College of Mechanical and Electrical Engineering, Hunan University of Science and Technology, Xiangtan 411201, China

Gareth J. Bennett[**]
School of Engineering, Trinity College Dublin, the University of Dublin, D02 PN40, Ireland

[*] Associated professor, Key Lab of Aerodynamic Noise Control, CARDC, corresponding author, zhaokun@cardc.cn.

[†] Postgraduate student, Key Lab of Aerodynamic Noise Control, CARDC.

[‡] Postgraduate student, School of Information Science and Engineering, Shenyang University of Technology.

[§] Associated Professor, College of Mechanical and Electrical Engineering, Hunan University of Science and Technology.

[**] Associated Professor, School of Engineering, Trinity College Dublin, AIAA Senior.

Abstract

Turbulent-boundary-layer wall-pressure-fluctuations are of significant concern in acoustic engineering for both high-speed airborne and underwater vehicles, and the modeling of the associated wavenumber-frequency spectra have been extensively studied. In this paper, a review of 12 models developed between 1964 and 2017 is conducted. Both the 2D and the 1D forms are investigated. In this work, fundamental concepts are introduced, followed by a classification of the models into two categories, i.e. Corcos-type and non-Corcos-type models. Both the 2D and 1D forms of the 12 models are individually introduced in chronological order. To evaluate these models, comparisons of the 2D and 1D wavenumber-frequency spectra at different speeds and frequencies were conducted. Unlike Corcos-type models, non-Corcos-type models are grounded in a stronger theoretical foundation, with some models accurately reflecting acoustic region characteristics. Corcos-type models exhibit good consistency, though they require an auto-spectrum as a necessary input making them semi-empirical models. Besides, the models within the Corcos-type and the non-Corcos-type were also compared, respectively, a few important conclusions were accordingly made. The research output from this paper can provide an important practical engineering reference for studies associated with acoustic engineering such as aircraft cabin noise and submarine hydrodynamic noise.

Nomenclature

c_0	= speed of sound, m/s
$\mathbf{k}$	=3D wavenumber vector, defined as (k_1, k_2, k_3)
$\mathbf{k}_{13}$	=2D wavenumber vector in the streamwise and spanwise direction, defined as (k_1, k_3)
k_{13}	=magnitude of $\mathbf{k}_{13}$, i.e. $k_{13} = \lvert\mathbf{k}_{13}\rvert = \sqrt{k_1^2 + k_3^2}$
k_0	= acoustic wavenumber, ω / c_0
k_1, k_2, k_3	=wavenumber in the streamwise, normal and spanwise direction, rad/m
k_c	= convection wavenumber, ω / U_c
l	= distance measured from the leading edge of the flat plate in the flow direction, m
p	=fluctuation pressure, Pa
Re_l	= Reynolds numbers referred to l
$\mathbf{r}$	=3D position vector, defined as (x_1, x_2, x_3)
U_∞	= freestream velocity, m/s
U_c	= convection velocity, m/s
U_τ	= friction velocity, m/s
x_1, x_2, x_3	=coordinate in the streamwise, normal and spanwise direction, m
$\delta(x)$	= Dirac function
δ	= boundary layer thickness, m
δ^*	= boundary layer displacement thickness, m
θ	= boundary layer momentum thickness
ν	= kinematic viscosity, m^2/s
$\boldsymbol{\xi}$	=3D position difference vector, defined as (ξ_1, ξ_2, ξ_3)
$\boldsymbol{\xi}_{13}$	=2D position difference vector in the streamwise and spanwise direction, defined as (ξ_1, ξ_3)
ξ_1, ξ_3	= position difference in the streamwise and spanwise direction, m
ρ_0	= fluid density, kg/m^3
ω	=angular frequency, rad·Hz

I. Introduction

TURBULENT-boundary-layer wall-pressure-fluctuations (TBL-WPFs) are induced by eddies within a fully developed boundary layer in the vicinity of a solid planar surface/wall. TBL-WPFs, on the one hand, can directly produce noise as a significant acoustic noise source; on the other hand, as an excitation source of the structure vibration, can lead to indirect noise and structural fatigue [1,2]. Consequently, TBL-WPFs have been extensively investigated in the field of both high-speed airborne and underwater vehicles, e.g. aeroplanes, high-speed trains, submarines, etc[3–6]. TBL-WPFs are directly associated with turbulence so that they possess characteristics of randomness, unsteadiness and chaos, which require statistical measures to help describe them, such as the root mean square (RMS), the auto-power spectral density (auto-spectrum or frequency spectrum for short), the cross-power spectral density (cross-spectrum for short) and the wavenumber-frequency spectrum (abbreviated as W-F spectrum). Ther W-F spectrum, also termed wavevector-frequency spectrum, is capable of well describing TBL-

WPFs in both time and space domains. Therefore, as an effective excitation source expression, the W-F spectrum of TBL-WPFs has been extensively studied from the perspective of theory, experiment and numerical simulation[7–11].

Of the significant amount of research on the W-F spectrum of TBL-WPFs, the modeling of the W-F spectrum is a crucial topic. To date, from the earliest Corcos model[12,13] to the relatively new Doisy model[14], more than ten models have been proposed in almost sixty years of research. As the prediction capability of each model can largely differ from one another, a comparative study would be advantageous as a reference to both research and engineering fields. In the late 1990^{s}, a systematic work was performed by Graham[15]. In his comparison, the Corcos, Efimtsov, Smol'yakov-Tkachenko (also termed Smol'yakov I in this paper), John E. Ffowcs Williams (also termed FW-H-G in this paper) and ChaseI/II models were studied, and normalization was introduced to attain dimensionless W-F spectra to facilitate the comparison. Miller et al.[16] also investigated the differences in the Corcos, Mellen Elliptical, Chase I, and Smol'yakov I models by comparing them with experimental data. These two comparison works are of significance for reference to the TBL-WPFs study and application of the W-F spectrum, nonetheless, some drawbacks exist. Firstly, the studies by Graham[15] and Miller et al.[16] are merely limited to 6 classic models in total such as the Corcos and Chase I/II models, there are more models that are not included, especially those that appear in the 21st century, e.g. the Smol'yakov III and Doisy models. Secondly, some models require an input of the auto-spectrum (e.g. the Corcos model) while some do not (e.g. the Chase I/II models). In other words, the accuracy of the auto-spectrum plays a significant role in only some but not all models of the W-F spectrum, to which has not yet been paid enough attention. Thirdly, in many practical situations, only the W-F spectrum in the streamwise direction are of concern and measured[17,18], i.e. the 1D form the W-F spectrum. Nevertheless, the models in the literature are normally provided in the 2D form with both streamwise and spanwise direction, i.e. there is a lack of 1D form from many models. As such, the 1D form of each model is highly expected in this field and comparisons of the 1D form and the 2D form are both highly expected.

In this paper, 12 models of TBL-WPFs W-F spectra in both 2D and 1D forms are reviewed and compared in detail. The paper is organized as follows: in Section II an overall review of the 12 W-F spectral models is made. Initially, these models are classified into two categories according to their theoretical basis and expression form. Then, the original expressions of these models in the 2D form are introduced in detail. In Section III, the 1D form of these models are calculated by the authors based on the integration over the spanwise wavenumber range. Note that not all models are analytically integrable so numerical integration is also used for those. Section IV and

Section V compare the 2D and 1D models respectively, and an evaluation of each model is provided. In Section VI, conclusions are according presented.

II. Review of W-F spectral models for TBL-WPFs in 2D form

A. Fundamental concept

For two arbitrary points on a TBL wall, whose positions can be denoted as $\mathbf{r}$ and $\mathbf{r}+\boldsymbol{\xi}$, the TBL-WPFs can be written as $p(\mathbf{r},t)$ and $p(\mathbf{r}+\boldsymbol{\xi},t+\tau)$. The corresponding time-space correlation function of the TBL-WPFs at these two points can be written as:

$$R(\mathbf{r},\mathbf{r}+\boldsymbol{\xi},t,t+\tau)=< p^{*}(\mathbf{r},t)p(\mathbf{r}+\boldsymbol{\xi},t+\tau)> \tag{1}$$

"< >" denotes an ensemble average, which is the expectation of a physical quantity in statistics. For a stationary and homogenous process, which is a fundamental assumption for TBL-WPFs studies, the time-space correlation function will be independent of $\mathbf{r}$ and t, i.e.:

$$R(\mathbf{r},\mathbf{r}+\boldsymbol{\xi},t,t+\tau)=R(\boldsymbol{\xi},\tau) \tag{2}$$

The cross-spectrum can be obtained from $R(\boldsymbol{\xi},\tau)$ via a Fourier transform in the time domain (See Appendix A):

$$\Phi(\boldsymbol{\xi},\omega)=\frac{1}{2\pi}\int_{-\infty}^{\infty}R(\boldsymbol{\xi},\tau)e^{-i\omega\tau}d\tau \tag{3}$$

When $\boldsymbol{\xi}$ is zero, which means the two points are coincident, then $\Phi(\boldsymbol{\xi},\omega)$ will become the auto-spectrum $\Phi(\omega)$. The auto-spectrum is one of the most important characteristics for TBL-WPFs, and currently, it is used as frequently as the W-F spectrum. However, as the focus of this paper is the W-F spectrum, we will not discuss in detail the $\Phi(\omega)$ other than how it is used to calculate the W-F spectrum. If $\Phi(\omega)$ is integrated over the angular frequency domain ω and the square root of the result is made, the RMS can be obtained:

$$\sqrt{\overline{p^2}}=\left(\int_{-\infty}^{\infty}\Phi(\omega)d\omega\right)^{\frac{1}{2}} \tag{4}$$

Alternatively, the W-F spectrum is obtained from the generalized Fourier transform in both the time and space domain of $R(\boldsymbol{\xi},\tau)$:

$$\Phi(\mathbf{k},\omega)=\frac{1}{(2\pi)^{n+1}}\int_{-\infty}^{+\infty}\int_{-\infty}^{+\infty}R(\boldsymbol{\xi},\tau)e^{-i(\mathbf{k}\cdot\boldsymbol{\xi}+\omega\tau)}d\boldsymbol{\xi}d\tau \tag{5}$$

, where n is the dimension of $\boldsymbol{\xi}$. In the study of TBL-WPFs, only k_1 and k_3 are considered, so $\boldsymbol{\xi}$ is replaced by $\boldsymbol{\xi}_{13}$, $\mathbf{k}$ is replaced by $\mathbf{k}_{13}$ with n =2.

There is another way to calculate the W-F spectrum. To begin with, the space-time Fourier transform of the TBL-WPFs can be obtained instead of $R(\boldsymbol{\xi}_{13},\tau)$, i.e.:

$$\hat{p}(\mathbf{k}_{13},\omega)=\frac{1}{(2\pi)^3}\int_{-\infty}^{+\infty}\int_{-\infty}^{+\infty}p(\mathbf{r}_{13},t)e^{-i(\mathbf{k}_{13}\cdot\mathbf{r}_{13}+\omega t)}d\mathbf{r}_{13}dt \tag{6}$$

Then, the W-F spectrum $\Phi(\mathbf{k}_{13},\omega)$ and $\hat{p}(\mathbf{k}_{13},\omega)$ have the relationship below:

$$<\hat{p}(\mathbf{k}_{13},\omega),\hat{p}^*(\mathbf{k}'_{13},\omega')>=\Phi(\mathbf{k}_{13},\omega)\delta(\mathbf{k}_{13}-\mathbf{k}_{13}')\delta(\omega-\omega') \tag{7}$$

, which can be used to calculate $\Phi(\mathbf{k}_{13},\omega)$. Note that $\delta(x)$ here is the Dirac function. With the Dirac delta function to make the selection, i.e.:

$$\int_0^\infty \delta(x-x')f(x')dx' = f(x) \tag{8}$$

Then, the W-F spectrum can be written as:

$$\Phi\left(\mathbf{k}_{13},\omega\right)=\int_{-\infty}^{+\infty}\int_{-\infty}^{+\infty}\left\langle\hat{p}\left(\mathbf{k}_{13},\omega,0\right)\hat{p}^*\left(\mathbf{k}'_{13},\omega',0\right)\right\rangle \mathrm{d}\mathbf{k}'_{13}\mathrm{d}\omega' \tag{9}$$

Fig. 1 provides three schematics of the TBL-WPFs W-F spectrum in different dimensions. As illustrated in Fig. 1(a), the W-F spectrum consists of the hydrodynamic component and the acoustic component, bounded by the acoustic cone. The acoustic component is mainly correlated with compressibility of the fluid, and the acoustic cone is its main character, defined by $k_1^2+k_3^2=k_0^2$. By contrast, the convective ridge, the peak that shows up at $(k_c,0)$, is the main character of the hydrodynamic component. When extracting a 2D section from Fig. 1(a) at certain ω, we will attain Fig. 1(b), i.e. the 2D schematic of the W-F spectrum, with more information provided. More specifically, the W-F spectrum can be subdivided into the acoustic region, the subconvective region (also termed as low-wavenumber region), the convective region and the viscous region[19]. Note that for supersonic flow, inside the range of the acoustic region there will be part of the hydrodynamic component as well, i.e. supersonic region, here we only focus on subsonic flow so it will be not discussed. As the peak of the convective region, the convective ridge is still notable. When extracting a 1D section from Fig. 1(b) at $k_3=0$, we will attain Fig. 1(c). It is clearly marked out that the acoustic component consists of the acoustic region and the hydrodynamic component consists of the subconvective region, the convective region and the viscous region. The boundary of the acoustic region is characterized by k_0 , where there is a singular point represented by a small peak. Besides, it is worth noting that concerning incompressible flow, $c_0 \to \infty$ then $k_0 \to 0$, which means the singular point disappears with no obvious acoustic region. This is in agreement with the Kraichnan-Phillips theory[20] for the incompressible flow, i.e. when $\mathbf{k}_{13} \to 0$ then $\Phi(\mathbf{k}_{13}, \omega) \to 0$, which is illustrated in Fig. 1(c). By contrast, when the compressibility is taken into account, the scenario will be much different, $\Phi(\mathbf{k}_{13}, \omega) \to 0$ will be not reached.

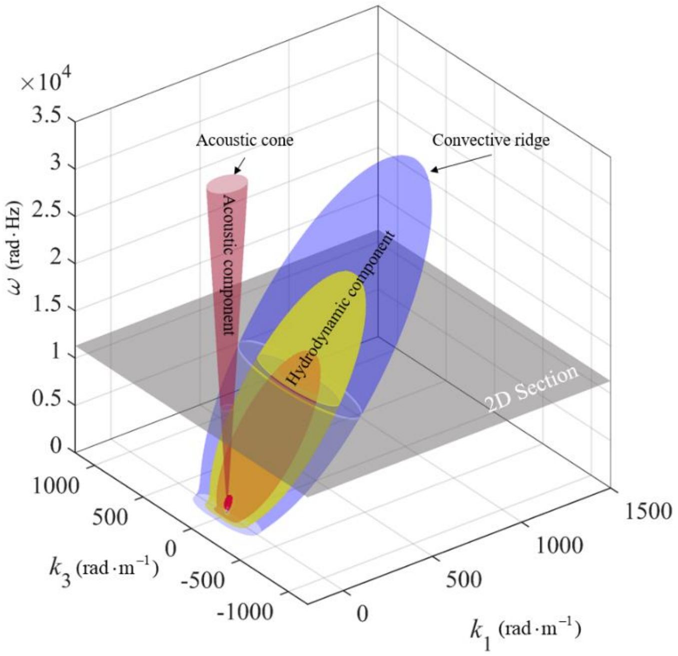

(a) 3D schematic

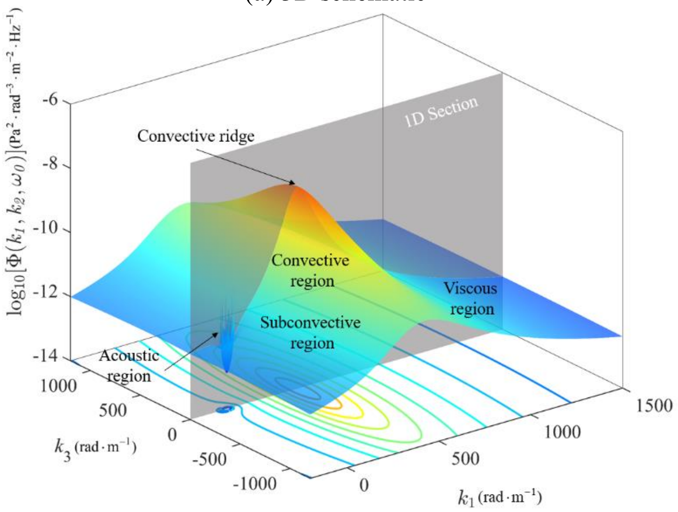

(b) 2D schematic (@ certain ω)

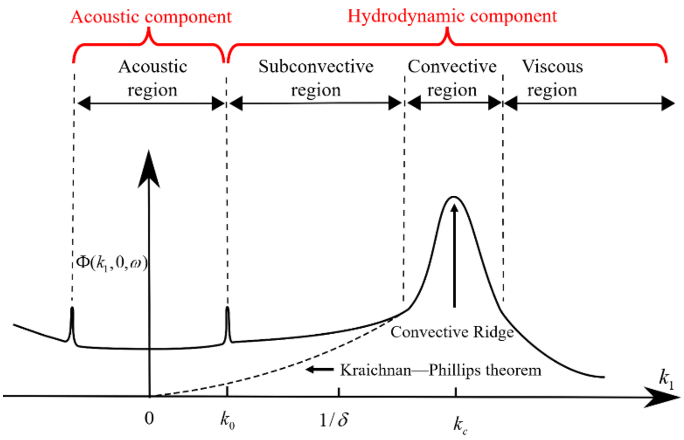

(c) 1D schematic (@ $k_3 = 0$)

Fig. 1 Schematics of TBL wall pressure W-F spectrum

As previously mentioned, the TBL-WPFs will produce direct noise, as well as indirect noise from flow-induced vibration. The acoustic region is mainly associated with direct noise production, and the convective and the subconvective regions are mainly associated with indirect noise. For instance, regarding the relatively high speed subsonic flow, e.g. flow associated with aircraft and high-speed train cabin noise, wavenumbers in the convective region tend to match those of the bending waves in the underlying structures; by contrast, regarding the relatively low speed subsonic flow associated with marine applications, wavenumbers in the convective region are too high and the structural wavelengths of interest lie in the subconvective portion of the W-F spectrum[21]. The viscous region is closely associated with viscosity, since the wavenumber is very high and that viscosity is frequently not considered, so research on this region is rare. It is worth noting that the 2D W-F spectrum models of TBL-WPFs discussed in this paper were developed to predict the surface in Fig. 1(b), while the 1D W-F spectrum discussed in this paper is absolutely not the curve in Fig. 1(c). Instead, the 1D W-F spectrum is the integral of the 2D W-F spectrum along k_3 from $-\infty$ to ∞, which will be further discussed in Section III.

B. Categories of the W-F spectral models

It has been almost sixty years since the birth of the first W-F spectral model for TBL-WPFs, namely the Corcos model. Admittedly, the proposal of a W-F spectral model requires complex theoretical investigation and a large amount of experimental data. As a result, some models with a history of over half a century are still in wide use, although there may exist obvious errors from the perspective of modern times. With the rapid development of experimental techniques and CFD simulation, surface array measurement technology and DNS in particular, more accurate data are expected to be used to support the new birth of more accurate models. However, the real bottleneck remains due to the relatively slow progress in theoretical development. In addition, it is worth noting that, to date, almost all models are made assuming flow over an infinitely long plate. This is due to the extra complexity when effects from other geometrical details are considered, which is an obvious drawback also. The models listed below all assume flow over an infinitely long plate.

Table 1. List of the considered W-F spectra prediction models for TBL-WPFs

No.	Model Name	Year	Country	Institution
1	Corcos [12,13]	1964	USA	University of California, Berkeley
2	Chase I[22]	1980	USA	Bolt Beranek and Newman Inc.
3	Efimtsov[23]	1982	USSR	TsAGI
4	FW-H-G[24,25]	1984	UK	University of Cambridge
5	Witting[26]	1986	USA	ORI Inc.
6	Chase II[27]	1987	USA	Chase Inc.
7	Mellen Elliptical[28,29]	1990	USA	Kildare Corp.
8	Smol'yakov-Tkachenko (also referred to Smol'yakov I)[30]	1991	USSR	Krylov Central Research Institute
9	TNO[31,32]	1998	The Netherlands	TNO
10	Smol'yakov II[33]	2000	Russia	Krylov Central Research Institute
11	Smol'yakov III[34]	2006	Russia	Krylov Central Research Institute
12	Doisy[14]	2017	France	Thales Underwater Systems SAS

Table 1 provides 12 W-F spectrum prediction models that were proposed between the years 1964~2017. From a comprehensive consideration of the theoretical basis and model expression, the authors classify these models into two categories: Corcos-type and non-Corcos-type models, shown in Fig. 2.

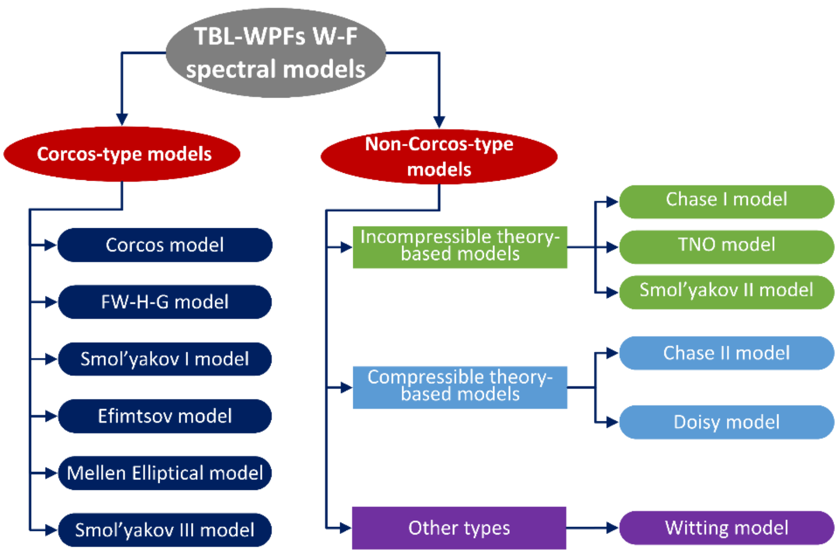

Fig. 2 Category of the TBL-WPFs W-F spectral models

(1) Corcos-type models

Models of this type are semi-empirical and consist of the classic Corcos model and all other models developing from the Corcos model, i.e. the FW-H-G model, Efimtsov model, Mellen Elliptical model, Smol'yakov-Tkachenko model and the Smol'yakov III model. All Corcos-type models contain the distinguishing feature that an auto-spectrum input of $\Phi(\omega)$ is required in the expression. More specifically, the accuracy of $\Phi(\omega)$ plays an important role in the prediction of the W-F spectrum for the Corcos-type models.

(2) Non-Corcos-type models.

In contrast to Corcos-type models are the models which do not need an input of $\Phi(\omega)$ and which can directly predict the W-F spectrum. Due to the theoretical foundation, the Non-Corcos-type models can be subdivided into the incompressible theory-based models, the compressible theory-based models and the others. The incompressible theory-based models are derived from the incompressible fluid equation, i.e. the Poisson equation, and ignore the compressibility effect of the fluid. These models include the Chase I model, the TNO model and the Smol'yakov II model. The compressible theory-based models are derived from the compressible fluid equation, and the effects of the fluid compressibility are taken into consideration. These models consist of the Chase II model and the Doisy model. Note that the compressibility is closely correlated with the acoustic region, so theoretically without compressibility it will be impossible to predict the acoustic region. The others include models that were derived using a different theory from the two above. In Table 1, only the Witting model belongs to this third subcategory.

C. Brief introduction to each model

Prior to introduction to each model, it is worth noting that almost all models here are the original forms from the literature, although, some models have been improved since they were developed. For a fair evaluation in the subsequent sections of this paper, such improvements are not considered.

(1) Corcos model

The earliest W-F spectrum model is the Corcos model, developed in 1964[12], and is still widely used in the study of TBL-WPFs[35]. As previously stated, many subsequent researchers have derived new models from the Corcos model. Before the establishment of the W-F spectrum model, Corcos[12] first started with modelling the time-space correlation function, i.e. Eq.(1). It was believed by Corcos[12] that the time domain Fourier transform of the time-space correlation function can be written as the product of the auto-spectrum and the decoupled exponential variation functions in the streamwise and spanwise directions. After the model was obtained using experimental data fitting, Corcos performed a generalized Fourier transform in the space domain, and then the W-F spectrum was obtained. The time domain Fourier transform of the time-space correlation function can be expressed as[12,13,36]:

$$R(\omega, x_1, x_3) = \Phi(\omega) A\left(k_c x_1\right) B\left(k_c x_3\right) e^{k_c x_1} \tag{10}$$

, where *A* and *B* are the exponential functions of $k_c x_1$ and $k_c x_3$. Regarding Eq.(10), Bull[37] attained the fitting from experimental data in 1967:

$$R(\omega, x_1, x_3) = \Phi(\omega) e^{-\alpha_1 |k_c x_1|} e^{-\alpha_3 |k_c x_3|} e^{i k_c x_1} \tag{11}$$

, where α_1 and α_3 are dependent on the roughness of the model surface. For a smooth surface, values by Bull[37] are 0.1 and 0.715. With the calculation approach shown in Eq.(5), the integral of Eq.(11) over the space domain is the W-F spectrum, expressed as:

$$\Phi(\mathbf{k}_{13}, \omega) = \Phi(\omega) \frac{\alpha_1 \alpha_3}{\pi^2 k_c^{\,2} [\alpha_1^{\,2} + (k_1 / k_c - 1)^2][\alpha_3^{\,2} + (k_3 / k_c)^2]} \tag{12}$$

In this paper, key coefficients of the Corcos model, i.e. α_1 and α_3, are set to be the same as Bull's [37] results, namely 0.1 and 0.715.

(2) Chase I model

D.M. Chase[22,38,27] proposed two classic models, i.e. the Chase I and Chase II models. Here Chase I [22] is first introduced. The Chase I model is based on the incompressible Poisson equation and uses the two source terms of the TBL-WPFs model originally defined by Kraichnan[20,39], namely:

$$\frac{1}{\rho_0} \nabla^2 p = -(T^{MT} + T^{TT}) \tag{13}$$

T^{MT} is called an MT term, whose full name is the Mean shear-Turbulence term (also known as the Linear term or the Rapid term). Assuming the velocity of the fluid is written as $\{U_1(x_2) + u_1, u_2, u_3\}$, where U_1 and u_i are the mean and the fluctuating components within the TBL, respectively, for TBL-WPFs, Kraichnan[20,39] developed the main source term to be:

$$T^{MT} = 2 \frac{\partial U_1}{\partial x_2} \frac{\partial u_2}{\partial x_1} \tag{14}$$

T^{TT} is the TT term, whose full name is the Turbulence-Turbulence term (also known as the Nonlinear term or the Slow term), T^{TT} is expressed as:

$$T^{TT} = T_{ij}^{\ TT} = \frac{\partial^2}{\partial x_i \partial x_j}\left(u_i u_j - \overline{u_i u_j}\right) \tag{15}$$

The derivation by Chase [22]shows that the component from T^{MT} in the W-F spectrum can be written as:

$$\Phi_{MT}(\mathbf{k}_{13},\omega) = 4\rho_0^{\ 2}\frac{k_1^{\ 2}}{k_{13}^{\ 2}}\int_0^\infty dx_2 \int_0^\infty dx_2' e^{-k_{13}(x_2+x_2')}\frac{dU_1(x_2)}{dx_2}\frac{dU_1(x_2')}{dx_2'}E_{22}\left(x_2, x_2', \mathbf{k}_{13}, \omega\right) \tag{16}$$

, where:

$$E_{22}\left(x_2, x_2', \mathbf{k}_{13}, \omega\right) = \frac{\mathrm{E}\left[u_2(x_2,\mathbf{k}_{13},\omega)u_2^{\ *}\left(x_2', \mathbf{k}_{13}', \omega'\right)\right]}{\delta\left(\mathbf{k}_{13}' - \mathbf{k}_{13}\right)\delta\left(\omega' - \omega\right)} \tag{17}$$

$E_{22}\left(x_2, x_2', \mathbf{k}_{13}, \omega\right)$ represents the cross-spectrum of the space-time domain Fourier transform of the velocity fluctuation normal component in different normal layers. The component corresponding to T^{TT} can be denoted as:

$$\Phi_{TT}(\mathbf{k}_{13},\omega) = \frac{\rho_0^{\ 2}}{k_{13}^{\ 2}}\int_0^\infty dx_2 \int_0^\infty dx_2' e^{-k_{13}(x_2+x_2')} S\left(x_2, x_2', \mathbf{k}_{13}, \omega\right) \tag{18}$$

, where:

$$S\left(x_2, x_2', \mathbf{k}_{13}, \omega\right) = \frac{\mathrm{E}\left[\hat{T}^{TT*}(x_2,\mathbf{k}_{13},\omega)\hat{T}^{TT}\left(x_2', \mathbf{k}_{13}', \omega'\right)\right]}{\delta\left(\mathbf{k}_{13}' - \mathbf{k}_{13}\right)\delta\left(\omega' - \omega\right)} \tag{19}$$

$S\left(x_2, x_2', \mathbf{k}_{13}, \omega\right)$ represents the cross-spectrum of the space-time domain Fourier transform of the TT term in different normal layers. By theoretical analysis associated with experimental data, Chase succeeded in the direct modelling of E_{22}, S and dU_1 / dx_2 in Eq.(16) and Eq.(18), such that the Chase I model can be written as：

$$\Phi(\mathbf{k}_{13},\omega) = \Phi_{MT}(\mathbf{k}_{13},\omega) + \Phi_{TT}(\mathbf{k}_{13},\omega) = \rho_0^{\ 2} U_\tau^{\ 3}\left(C_{MT}k_1^2 K_{MT}^{-5} + C_{TT}k_{13}^{\ 2}K_{TT}^{-5}\right) \tag{20}$$

, where:

$$K_i^2 = \frac{\left(\omega - U_c k_1\right)^2}{h_i^2 U_\tau^{\ 2}} + k_{13}^{\ 2} + \left(b_i\delta\right)^{-2}, i = MT, TT \tag{21}$$

In this paper, key coefficients of the Chase I model, i.e. C_{MT}, C_{TT}, b_{MT}, b_{TT}, h_{MT}, h_{TT} were set to be 0.0745, 0.0475, 0.756, 0.378, 3.0, 3.0 [15].

(3) Efimtsov model

Developed in 1982, the Efimtsov model[23] continued the use of the Corcos modelling approach and took the effects of boundary layer thickness δ and Mach number Ma on TBL-WPFs into consideration. From the Efimtsov model, the W-F spectrum can be predicted as:

$$\Phi(\mathbf{k}_{13},\omega)=\Phi(\omega)\frac{\Lambda_1\Lambda_3}{\pi^2\left[1+\left(k_1-k_c\right)^2\Lambda_1^2\right]\left[1+\left(k_3\Lambda_3\right)^2\right]} \tag{22}$$

Note that in the original reference, a dimensionless number $Sh=\omega\delta/U_\tau$ was used. Here in Eq. (22) we make a replacement for a simpler explicit expression. From the experiment, the Efimtsov model obtained the following expressions:

$$\frac{\Lambda_1}{\delta}=1/\sqrt{\left(a_1k_c\delta\right)^2+a_2^2/\left[\left(\omega\delta/U_\tau\right)^2+\left(a_2/a_3\right)^2\right]} \tag{23}$$

$$\begin{cases}\dfrac{\Lambda_3}{\delta}=1/\sqrt{\left(a_4k_c\delta\right)^2+a_5^2/[\left(\omega\delta/U_\tau\right)^2+\left(a_5/a_6\right)^2]},Ma<0.75\\ \dfrac{\Lambda_3}{\delta}=1/\sqrt{\left(a_4k_c\delta\right)^2+a_7^2},Ma>0.9\end{cases} \tag{24}$$

. It is worth noting that the Efimtsov model does not cover the Mach number range of 0.75~0.9.

In this paper, the key coefficients of the Efimtsov model $a_1 \sim a_7$ are set to be 0.1, 72.8, 1.54, 0.77, 548, 13.5 and 5.66 [15].

(4) FW-H-G model

The concept of FW-H-G was first proposed by the world renowned aeroacoustic scientist– John E. Ffowcs Williams[24]. Based on the Lighthill equation and acoustic analogy theory[40], John E. Ffowcs Williams extended his earlier research on time delay effects due to fluid compressibility[41] to the construction of W-F spectrum modelling, and combined these results with the Corcos model. As a consequence, a new semiempirical model that considers the Mach number variation was achieved. Nonetheless, because there are a few unknown functions and coefficients that require confirming, to date this model has not yet been directly in use. In 1984, after ignoring the compressibility again by setting Ma=0, Hwang and Geib[25] determined all the functions and coefficients by experiment. The final expression of the model is:

$$\Phi(\mathbf{k}_{13},\omega)=\Phi(\omega)\left(\frac{\mathbf{k}_{13}}{k_c}\right)^2\frac{\alpha_1\alpha_3}{\pi^2k_c{}^2[\alpha_1{}^2+(\frac{k_1}{k_c}-1)^2][\alpha_3{}^2+(\frac{k_3}{k_c})^2]} \tag{25}$$

In the review paper by Graham[15], this model was termed the Ffowcs Williams model . However, without the work by Hwang and Geib[25], this model would not be used in practice today so their contribution cannot be neglected. Accordingly, in this paper, the model was termed the FW-H-G model.

In this paper, the key coefficients of the FW-H-G model are set to be as same as the Corcos model, i.e. α_1 and α_3 are equal to 0.1 and 0.715 respectively.

(5) Witting model

The Witting model was developed in 1986[41], although for incompressible flow, it possesses significant differences from other Non-Corcos-type models in terms of the supporting theory. Witting[41] believed that the generation of TBL-WPFs is closely correlated to the burst and sweep phenomena of the turbulent boundary layer. Accordingly, as a type of dipole source, Witting first modelled the two phenomena using a stochastic method, thereby realizing the modelling of the TBL-WPFs W-F spectrum. In the study of the boundary layer, the burst was initially discovered by Kline et al[43] in 1967, when they used the hydrogen bubble to visualize the coherent motions in the inner layer of the turbulent boundary layer. The burst indicates the transient disturbance of the velocity inside the boundary layer, which is generally caused by wall friction. In the summary by Robinson[44], the sweep is one of the eight turbulent boundary wall coherent structures. More specifically, when fluid with higher velocity moves in the streamwise direction in the boundary layer, some low-velocity fluid will be entrained. Such a type of entrainment is termed as the sweep, which can result in various vortices and have substantial effects on the transport and mix of the boundary layer flow.

In the process of modelling, Witting[41] started by treating a single burst or sweep as an "event", and the W-F spectrum was treated as the summation of the products of numerous such wall pressure fluctuations induced by those events and their respective coefficients. Note that this summation can be replaced by an integral. Then, the Witting model transformed the integral into another one that integrates a fluctuation pressure correlation function over some normal height range. Finally, after some mathematical transformations, the model is written as:

$$\Phi(\mathbf{k}_{13},\omega) = \frac{8}{3}\overline{p^2}\frac{\delta^{*3}}{U_c}\frac{A\hat{\omega}^2}{\xi^5}\int_{\xi_{\min}}^{\xi_{\max}} {x_2}^4 e^{-2x_2}\,dx_2 \tag{26}$$

, where:

$$\begin{cases} \xi = \hat{k}_{13} + C\left|\hat{\omega} - \hat{k}_1\right| \\ \xi_{max} = \dfrac{\xi\delta_{max}}{\delta^*},\ \xi_{\min} = \dfrac{\xi\delta_{\min}}{\delta^*} \\ \hat{k}_1 = k_1\delta^*,\ \hat{k}_3 = k_3\delta^*, \hat{k}_{13} = \sqrt{\hat{k}_1^{\ 2} + \hat{k}_3^{\ 2}} \\ \hat{\omega} = \dfrac{\omega\delta^*}{U_c}, A = \dfrac{C}{\pi}\dfrac{1}{(1+\dfrac{2}{3C^3})\ln\dfrac{\delta_{max}}{\delta_{min}}} \end{cases} \tag{27}$$

The mean square $\overline{p^2}$ was modelled as：

$$\overline{p^2} = 0.015 U_c^{\ 2} U_\tau^{\ 2} \rho_0^{\ 2} \tag{28}$$

In this paper, the key coefficients of the Witting model, C, δ_{max} and δ_{min} are set to be 8, $\delta_{max} = 8\delta^*$ and $\delta_{min} = 0.005\delta^*$ [41].

(6) Chase II model

The Chase II model was proposed in 1987[27] by the same creator of the Chase I model, i.e. D.M. Chase. Compared with the Chase I model, the Chase II model made a significant improvement by taking the compressibility of the fluid into account. More specifically, the Chase II model was derived from the dimensionless approach based on the low wavenumber and low Mach number assumptions by Bergeron[45], and the expression of the TBL-WPFs can be written as:

$$\hat{p}(\mathbf{k}_{13},\omega) = -\rho_0 k_{13}\int_0^\infty dx_2 e^{(-K_c x_2)}\{\frac{k_{13}}{K_c}\hat{T}'_{33} - \frac{K_c}{k_{13}}\hat{T}'_{22} + i2\left[\frac{k_1}{K_c}\frac{dU_1(x_2)}{dx_2}\frac{1}{\omega} - 1\right]\hat{T}'_{32}\} \tag{29}$$

, where $\hat{T}'_{33}$, $\hat{T}'_{22}$ and $\hat{T}'_{32}$ are the components of the mentioned T^{TT} in Eq.(13) after a transformation of coordinates. The core of this transformation is related to the source term. More specifically, let (x_1, x_2, x_3) be a rotated coordinate system such that x_3 lies along $\mathbf{k_{13}}$ [46,47]. Besides,

$$K_c = \begin{cases} -i\sqrt{k_0^{\ 2} - k_{13}^{\ 2}}, k_{13} < \omega / c_0 \\ \sqrt{k_{13}^{\ 2} - k_0^{\ 2}}, k_{13} > \omega / c_0 \end{cases} \tag{30}$$

Likewise, the Chase II model also divided the W-F spectrum into an MT and TT term, namely:

$$\begin{cases} \Phi_{MT}(\mathbf{k}_{13},\omega) = 4\rho_0^{\,2}\dfrac{k_1^{\,2}k_{13}^{\,2}}{\omega^2 K_c^{\,2}}\displaystyle\int_0^{\infty} dx_2 \int_0^{\infty} dx_2' e^{-K_c^* x_2 - K_c x_2'}\dfrac{dU_1(x_2)}{dx_2}\dfrac{dU_1(x_2')}{dx_2'} S'_{32}\left(x_2, x_2', \mathbf{k}_{13}, \omega\right) \\ \Phi_{TT}(\mathbf{k}_{13},\omega) = \rho_0^{\,2} k_{13}^{\,2}\displaystyle\int_0^{\infty} dx_2 \int_0^{\infty} dx_2' e^{-K_c^* x_2 - K_c x_2'} \ldots \\ \ldots\{\dfrac{k_{13}^{\,2}}{K_c^{\,2}} S'_{33}\left(x_2, x_2', \mathbf{k}_{13}, \omega\right) + \dfrac{K_c^{\,2}}{k_{13}^{\,2}} S'_{22}\left(x_2, x_2', \mathbf{k}_{13}, \omega\right) + 4S'_{32}\left(x_2, x_2', \mathbf{k}_{13}, \omega\right)\} \end{cases} \tag{31}$$

, where $S'_{ij}\left(x_2, x_2', \mathbf{k}_{13}, \omega\right)$ is the component of $S\left(x_2, x_2', \mathbf{k}_{13}, \omega\right)$ in Eq.(19), but after a transformation of coordinates. With simplification, the final expression of the Chase II model, as the sum of all equations in Eqs.(31), is written as:

$$\Phi(\mathbf{k}_{13},\omega) = \frac{\rho_0^{\,2} U_\tau^{\,3}}{\left[K_+^2 + (b\delta)^{-2}\right]^{5/2}}\{[c_2\left(\frac{|K_c|}{k_{13}}\right)^2 + c_3\left(\frac{k_{13}}{|K_c|}\right)^2 + 1 - c_2 - c_3]C_{TT} k_{13}^{\,2}[\frac{K_+^2 + (b\delta)^{-2}}{k_{13}^{\,2} + (b\delta)^{-2}}] + C_{MT}(\frac{k_{13}}{|K_c|})^2 k_1^2\} \tag{32}$$

and:

$$K_+^2 = \frac{\left(\omega - U_c k_1\right)^2}{h^2 U_\tau^{\,2}} \tag{33}$$

In this paper, the key coefficients of the Chase II model, including c_2, c_3, C_{TT}, C_{MT} and h, are 1/6, 1/6, 0.0047, 0.155, 3.0[27].

(7) Mellen Elliptical model

To avoid irregularity of the W-F spectrum, Mellen[28,29] held the opinion that the correlation function in the Corcos model can be expressed as the elliptical form instead of the exponential form, namely:

$$R(\omega, x_1, x_3) = \Phi(\omega) e^{-\sqrt{(\alpha_1 k_c x_1)^2 + (\alpha_3 k_c x_3)^2}} e^{i k_c x_1} \tag{34}$$

With a Fourier transform in the space domain, the W-F spectrum can be obtained from Eq.(34) as:

$$\Phi(\mathbf{k}_{13},\omega) = \Phi(\omega)\frac{(\alpha_1\alpha_3 k_c^{\,2})^2}{2\pi\left[(\alpha_1\alpha_3 k_c^{\,2})^2 + (\alpha_1 k_3 k_c)^2 + \alpha_3^{\,2} k_c^{\,2}(k_1 - k_c)^2\right]^{3/2}} \tag{35}$$

In this paper, key coefficients of the Mellen Elliptical model, i.e. α_1 and α_3, were set to be as same as the Corcos model.

(8) Smol'yakov-Tkachenko model(Smol'yakov I)

The Smol'yakov-Tkachenko model[30], also referred to as the Smol'yakov I model is an improvement to the classic Corcos model from a few different perspectives. Similar to the Mellen Elliptical model it also uses an elliptical form to express the correlation function. The model also partially adopts the ideas of the Efimtsov approach and establishes the connection between the correlation function and the boundary layer thickness. To improve the prediction of the subconvective region without sacrificing other wavenumber regions, in particular the convective region, the Smol'yakov I model includes extra corrections. The final expression of the model is written as:

$$\Phi(\mathbf{k}_{13},\omega)=\Phi(\omega)\frac{0.974}{(2\pi k_c)^2}A(\omega)h(\omega)[F(\mathbf{k}_{13},\omega)-\Delta F(\mathbf{k}_{13},\omega)] \tag{36}$$

, where:

$$\begin{cases} A(\omega)=0\cdot 124\left[1-\frac{1}{4k_c\delta^*}+\left(\frac{1}{4k_c\delta^*}\right)^2\right]^{1/2} \\ h(\omega)=\left[1-\frac{m_1 A}{6\cdot 515\sqrt{G}}\right]^{-1} \\ m_1=\frac{1+A^2}{1\cdot 025+A^2} \\ G=1+A^2-1.005m_1 \\ F(\mathbf{k}_{13},\omega)=\left[A^2+\left(1-\frac{k_1}{k_c}\right)^2+\left(\frac{k_3}{6\cdot 45k_c}\right)^2\right]^{-3/2} \\ \Delta F(\mathbf{k}_{13},\omega)=0.995\{1+A^2+\frac{1.005}{m_1}[(m_1-\frac{k_1}{k_c})^2+(\frac{k_3}{k_c})^2-m_1{}^2]\}^{-\frac{3}{2}} \end{cases} \tag{37}$$

In this paper, all key coefficients of the Smol'yakov I model can be attained from the calculations in Eq.(37).

(9) TNO model

In 1998, Parchen[31] from TNO (Netherlands Organization for Applied Scientific Research) tried to establish a model to predict wind turbine broadband noise due to the interaction of the TBL and the airfoil trailing edge. Since TBL-WPFs are the dominant source of this noise type, modelling of the W-F spectra is a key step, which contributes to the development of the TNO model. The TNO mode has been one of the fastest developing models, improvement from different aspects has been made since its birth[32,48–50]. Similar to the Chase I model, the TNO model was also derived from the incompressible flow equations, but in the TNO model, the MT term was treated as the main component with the TT term ignored. Modelling of the MT term in the W-F spectrum begins with the term $\Phi_{MT}(\mathbf{k}_{13},\omega)$ in Eq. (16), and the TNO model first non-dimensionalized $E_{22}\left(x_2,x_2^{'},\mathbf{k}_{13},\omega\right)$ in the following way:

$$\tilde{E}_{22}\left(x_2,x_2^{'},\mathbf{k}_{13},\omega\right)=\frac{E_{22}\left(x_2,x_2^{'},\mathbf{k}_{13},\omega\right)}{\sqrt{\overline{u_2^2\left(x_2\right)u_2^{'2}\left(x_2^{'}\right)}}} \tag{38}$$

Using the separation of variables method, Blake[19] provides:

$$\tilde{E}_{22}\left(x_2, x_2^{'}, \mathbf{k}_{13}, \omega\right) = R_{22}(x_2 - x_2^{'})\tilde{\phi}_2\left(x_2, \mathbf{k}_{13}, \omega\right) \tag{39}$$

, where $R_{22}(x_2 - x_2^{'})$ stands for the cross-correlation function of different normal layers and $\tilde{\phi}_2\left(x_2, \mathbf{k}_{13}, \omega\right)$ is the non-dimensionalized result of the Fourier transform in both the time and frequency domain of the normal velocity fluctuation. Here, $R_{22}(x_2 - x_2^{'})$ can be written as:

$$R_{22}(x_2 - x_2^{'}) = \Lambda_2(x_2)\delta(x_2 - x_2^{'}) \tag{40}$$

, and $\Lambda_2(x_2)$ is the normal turbulence integral length scale. The term $\tilde{\phi}_2\left(x_2, \mathbf{k}_{13}, \omega\right)$, again using separation of variables[19], can be written as

$$\tilde{\phi}_2\left(x_2, \mathbf{k}_{13}, \omega\right) = \tilde{\phi}_2\left(x_2, \mathbf{k}_{13}\right)\phi(\omega - U_c k_1) \tag{41}$$

, where $\tilde{\phi}_2\left(x_2, \mathbf{k}_{13}\right)$ represents the non-dimensionalized wavenumber spectrum of the normal velocity fluctuation. The term $\phi(\omega - U_c(x_2)k_1)$ is the moving axis spectrum, which describes how $\tilde{\phi}_2\left(x_2, \mathbf{k}_{13}\right)$ migrates and distorts. Substituting Eqs. (38)~(41) into Eq.(16), we can get the main expression of the TNO model:

$$\begin{aligned}\Phi_{MT}(\mathbf{k}_{13}, \omega) = \frac{4\rho_0{}^2 k_1{}^2}{k_{13}{}^2}\int_0^{\infty} dx_2 \int_0^{\infty} dx_2^{'} e^{-k_{13}(x_2 + x'_2)} \frac{dU_1}{dx_2}\frac{dU_1}{dx_2^{'}}\sqrt{\overline{u_2^2\left(x_2\right)u_2^{'2}\left(x_2^{'}\right)}}\ldots \\ \ldots\Lambda_2(x_2)\delta(x_2 - x_2^{'})\tilde{\phi}_2\left(x_2, \mathbf{k}_{13}\right)\phi(\omega - U_c k_1)\end{aligned} \tag{42}$$

Using Eq.(8) to make the selection, Eq.(42) can be simplified as:

$$\Phi_{MT}(\mathbf{k}_{13}, \omega) = \frac{4\rho_0{}^2 k_1{}^2}{k_{13}{}^2}\int_0^{\infty} dx_2 e^{-2k_{13}x_2}\left(\frac{dU_1}{dx_2}\right)^2 \overline{u_2^2\left(x_2\right)}\Lambda_2(x_2)\tilde{\phi}_2\left(x_2, \mathbf{k}_{13}\right)\phi(\omega - U_c k_1) \tag{43}$$

Therefore, the TNO model requires expressing explicitly each term of Eq.(42), i.e. dU_1/dx_2, $\overline{u_2^2\left(x_2\right)}$, $\Lambda_2(x_2)$, $\tilde{\phi}_2\left(x_2, \mathbf{k}_{13}\right)$, $\phi(\omega - U_c k_1)$. In this paper, the modelling in detail, taken from references[49,51], is introduced below.

For dU_1/dx_2, the Cole law[52] is adopted:

$$U_1 = U_\tau\left(\frac{1}{\kappa}\ln\left(\frac{U_\tau x_2}{\nu}\right) + B + \frac{1}{2}W\left(\frac{U_\infty}{U_\tau} - \frac{1}{\kappa}\ln\left(\frac{U_\tau \delta}{\nu}\right) - B\right)\right) \tag{44}$$

, where the Von Karman constant and the empirical constant κ and B are 0.41 and 5.5 respectively. The wake function W is:

$$W = 1 - cos\left(\pi x_2/\delta\right) \tag{45}$$

For $\Lambda_2(x_2)$, generally an approximation is used such as:

$$\Lambda_2(x_2) = \frac{l_m}{\kappa} \tag{46}$$

, and the mixing length scale l_m is written as:

$$l_m = \frac{0.085\delta \tanh\left(\frac{\kappa x_2}{0.085\delta}\right)}{\sqrt{1+B(x_2/\delta)^6}} \tag{47}$$

The term $\overline{u_2^2(x_2)}$, is expressed as a function of the turbulent kinetic energy k_T :

$$\overline{u_2^2} = ck_T \tag{48}$$

, where c is a coefficient. In the case of an airfoil, the value of c for the suction side is 0.45, whereas it takes the value 0.3 for the pressure side. However, since the model of interest in this paper is that of a flat plate, we use 0.35 as a compromise. The term k_T can be calculated as:

$$k_T = \sqrt{v_t^2 (dU_1/dx_2)^2 / C_\mu} \tag{49}$$

, where C_μ is 0.09. v_t is the eddy viscosity, whose definition is from Prandtl's mixing-length theory:

$$v_t = l_m^2 |dU_1/dx_2| \tag{50}$$

For $\tilde{\phi}_2(x_2, \mathbf{k}_{13})$, in the early research by Parchen [31], the assumption of isotropy was adopted to do the modelling, which is in fact far from reality. Here, we use the corrected $\tilde{\phi}_2(x_2, \mathbf{k}_{13})$ term by Bertagnolio[53]:

$$\tilde{\phi}_2(x_2, \mathbf{k}_{13}) = \frac{4\beta_1\beta_3}{9\pi}\Lambda^2 \frac{(\beta_1\Lambda k_1)^2 + (\beta_3\Lambda k_3)^2}{[1+(\beta_1\Lambda k_1)^2 + (\beta_3\Lambda k_3)^2]^{7/3}} \tag{51}$$

, where β_1 and β_2 are the correction coefficients corresponding to the streamwise and the spanwise wavenumbers. These values are 1 and 0.9. The term Λ is the length scale of the energy-containing eddies, calculated using the following relationship:

$$\Lambda_2 = 0.747\Lambda \tag{52}$$

For $\phi(\omega - U_c k_1)$, the TNO model usually used a normal distribution function to express the moving axis spectrum, i.e.:

$$\phi = \frac{1}{\sigma\sqrt{2\pi}} e^{-\left[\frac{(\omega-\mu)}{2\sigma^2}\right]^2} \tag{53}$$

, where:

$$\begin{aligned} \mu &= U_c k_1 \\ \sigma &= \frac{0.05 U_c}{\Lambda_2} \end{aligned} \tag{54}$$

In this paper, all key coefficients of the TNO model can be attained for the calculation using Eqs.(44)~(54).

(10) Smol'yakov II model

Smol'yakov proposed a new model in 2000[33] based on an incompressible theory with only the MT term considered, i.e. Eq.(16). To begin with, the difference between x_2 and $x_2^{'}$ was ignored, and Eq.(16) can be rewritten as:

$$\Phi_{MT}(\mathbf{k}_{13},\omega) = \frac{4\rho_0{}^2 k_1{}^2}{k_{13}{}^2} \int_0^\infty \mathrm{d}x_2 e^{-2k_{13}x_2} (\frac{dU_1}{dx_2})^2 E_{22}\left(x_2,\mathbf{k}_{13},\omega\right) \tag{55}$$

, where $E_{22}\left(x_2,\mathbf{k}_{13},\omega\right)$ is $E_{22}\left(x_2,x_2^{'},\mathbf{k}_{13},\omega\right)$ after $x_2^{'}$ is substituted by x_2 . Though there is a lack of mathematical completeness, this step has often been taken in the modelling of TBL-WPFs. Smol'yakov holds the opinion that $E_{22}\left(x_2,\mathbf{k}_{13},\omega\right)$ can be expressed in the following form:

$$E_{22}\left(x_2,\mathbf{k}_{13},\omega\right) = B\left(x_2,\mathbf{k}_{13},\omega\right)\phi(\omega - U_c k_1) \tag{56}$$

The term $B\left(x_2,\mathbf{k}_{13},\omega\right)$ was modelled as:

$$B\left(x_2,\mathbf{k}_{13},\omega\right) = f(x_2)\left(k_1^2 + \beta^2 k_3^2\right) e^{\left\{-\alpha l\left[k_{13}+|k_1|(\beta-1)\right]\right\}} \tag{57}$$

, where l is the typical size of eddy structures, written as:

$$l = \overline{u_1 u_2}^{\frac{1}{2}} (\frac{dU_1}{dx_2})^{-1} \tag{58}$$

Regarding the function $f(x_2)$ in Eq.(57), there is a positive correlation relation:

$$f(x_2) \propto v_c l^5 \tag{59}$$

, where v_c is the characteristic value of the turbulence fluctuation velocity, defined as:

$$v_c \propto \overline{u_1 u_2}^{\frac{1}{2}} \tag{60}$$

Smol'yakov modelled l, v_c and dU_1 / dx_2 based on previous experimental conclusions, and obtained the following expressions:

$$v_c \propto U_\tau e^{-1.25x_2^2} \tag{61}$$

$$l = \frac{\delta}{\gamma} e^{1.25x_2^2} \tag{62}$$

$$\frac{dU_1}{dx_2} = \gamma \frac{U_\tau}{\delta} e^{-2.5{x_2}^2} \tag{63}$$

Assuming the coefficient of the positive correlation relation is A and substituting Eqs.(56)~(63) for Eq. (55), we can get the final expression of the Smol'yakov II model:

$$\begin{aligned} \Phi_{MT}(\mathbf{k}_{13},\omega) = \frac{4A{\rho_0}^2{k_1}^2}{{k_{13}}^2\gamma^3}\delta^3{U_\tau}^3\left(k_1^2+\beta^2k_3^2\right)\int_0^\infty dx_2 ... \\ ...\exp\{-\alpha\frac{\delta}{\gamma}e^{1.25x_2^2}\left[k_{13}+\left|k_1\right|(\beta-1)\right]-2k_{13}x_2\}\phi(\omega-U_ck_1) \end{aligned} \tag{64}$$

, where $\phi(\omega-U_ck_1)$ is as same as the Smol'yakov II model, i.e. Eq.(53).

In this paper, the key coefficients of the Smol'yakov II model, α , β , γ , A are set to be, according to Smol'yakov[33], $1/\pi$, 6, 17.9, 1.6 respectively.

(11) Smol'yakov III model

The Smol'yakov III model, appearing in 2006[34], is a more recent Corcos-type model developed by Smol'yakov. First of all, in the model the correlation function is optimized as:

$$R(\omega,x_1,x_3) = \Phi(\omega)[h\gamma e^{ix_1k_c} - (h-1)\Delta\gamma e^{im_1x_1k_c}] \tag{65}$$

, where:

$$\begin{aligned} &\gamma = e^{-\sqrt{(\frac{x_1}{\Lambda_1})^2+(\frac{x_3}{\Lambda_3})^2}}, \Delta\gamma = e^{-\sqrt{(\frac{x_1}{l_s})^2+(\frac{x_3}{l_s})^2}} \\ &\Lambda_1 = \frac{1}{k_cB}, \Lambda_3 = \frac{1}{k_cBm}, l_s = \frac{1}{k_c}\sqrt{\frac{n}{m_1G}} \\ &m_1 = \frac{(1+B^2)}{5n-4+B^2}, G = 1+B^2-nm_1 \\ &h = \frac{1}{1-\dfrac{m_1B}{m_0n^2G^{1/2}}}, m_0 = 6.45, n = 1.005 \end{aligned} \tag{66}$$

and:

$$B=\frac{A}{1+SA(\frac{\omega\nu}{U_\tau{}^2})(\frac{U_\tau}{U_\infty})(\frac{U_\infty}{U_c})}$$

$$A=0.124[1-0.25\frac{1}{k_c\delta^*}+(0.25\frac{1}{k_c\delta^*})^2]^{\frac{1}{2}} \tag{67}$$

$$\frac{U_c}{U_\infty}=\frac{1.6\left(\frac{\omega\delta^*}{U_\infty}\right)}{1+16\left(\frac{\omega\delta^*}{U_\infty}\right)^2}+0.6$$

Here, Λ_1 and Λ_3 are termed the coherence length scales. Using a Fourier Transform, the W-F spectrum can be obtained from Eq.(65) as:

$$\Phi(\mathbf{k}_{13},\omega)=\frac{\Phi(\omega)}{2\pi}\{\frac{h\Lambda_1\Lambda_3}{\left[1+\Lambda_1{}^2\left(k_c-k_1\right)^2+\left(\Lambda_3k_3\right)^2\right]^{3/2}}-\frac{(h-1)l_s{}^2}{\left[1+l_s{}^2\left(m_1k_c-k_1\right)^2+\left(l_sk_3\right)^2\right]^{3/2}}\} \tag{68}$$

According to the author, the Smol'yakov III model differs from other models in four ways [34]: I. The model of $\Phi(\omega)$ used in Smol'yakov III explicitly depends on the Reynolds number; II. The ratio of the convective velocity to the velocity of the incoming flow U_c/U_∞ is not considered to be constantly equal to $0.7U_\infty$ but rather using Eq.(67); III. The proposed model is expressed in terms of the coherence scales which makes it more convenient for practical calculations of flow noise and vibration; IV. The model considers a dependence on viscosity by introducing a coefficient *S*. Regarding *S*, Smol'yakov estimates the value to be in the range of 70~150 for air, therefore in the original reference, a compromise was made with *S*=100.

In this paper, the key coefficients of the Smol'yakov III model including *S*, m_0 and *n* are set to be 100, 6.45 and 1.005 respectively.

(12) Doisy model

Developed in 2017, the Doisy model[14] is the newest among all examined in this paper, and one of the two compressible theory-based models in addition to the Chase II model. The Doisy model is based on Lighthill's equation[40], and with the introduction of the compressible continuity equation and through transformation, a new governing equation can be obtained[54]:

$$\frac{1}{c_0^2}\frac{\partial^2 p}{\partial t^2}-\Delta p+\frac{\overline{U_1^2}}{c_0^2}\frac{\partial^2 p}{\partial x_1^2}+\frac{2\overline{U_1}}{c_0^2}\frac{\partial^2 p}{\partial x_1\partial t}=\rho_0\left[\underbrace{2\frac{\mathrm{d}\overline{U_1}}{\mathrm{d}x_2}\frac{\partial u_2}{\partial x_1}}_{T^{MT}}+\underbrace{\frac{\partial^2\left(u_iu_j\right)}{\partial x_i\partial x_j}}_{T^{TT}}\right] \tag{69}$$

On the left side of the governing equation is the convection term, and on the right side are the source terms. Doisy also classified the source terms on the right side of Eq.(69) into an MT term and a TT term. By applying a Fourier transform in both the time and space domain to Eq.(69), the following form is obtained:

$$\frac{\mathrm{d}^2 \hat{p}\left(\mathbf{k}_{13},\omega,x_2\right)}{\mathrm{d}{x_2}^2}+\left\{\frac{\left(\omega+k_1\overline{U_1}\right)^2}{c_0^2}-\mathbf{k}_{13}^2\right\}\hat{p}\left(\mathbf{k}_{13},\omega,x_2\right)=-\rho_0\left(\hat{T}^{MT}+\hat{T}^{TT}\right) \tag{70}$$

To better describe the properties of the source terms, Doisy expressed the equation in a reference coordinate system S' where there is no mean flow velocity. In this coordinate system, the origin moves along the flow direction at a constant velocity $\overline{U_1}\left(x_2\right)$. Thus, Eq(70) can be written as:

$$\frac{\mathrm{d}^2 \hat{p}\left(\mathbf{k}_{13},\omega,x_2\right)}{\mathrm{d}{x_2}^2}+\left\{\frac{\omega^2}{c_0^2}-\mathbf{k}_{13}^2\right\}\hat{p}\left(\mathbf{k}_{13},\omega,x_2\right)=-\rho_0\left(\hat{T}^{MT}+\hat{T}^{TT}\right) \tag{71}$$

Using an acoustic analogy approach, the convection and source terms of Eq.(71) can be decoupled, referring to the early work of John E. Ffowcs Williams [24]. Doisy conducted a few additional steps to model the source terms and to solve the convection term, and finally obtained the following WPF expression:

$$\begin{cases}\hat{p}_{MT}\left(\mathbf{k}_{13},\omega,0\right)=-\dfrac{2\rho_0 k_1}{\gamma}\displaystyle\int_0^{+\infty}\mathrm{e}^{\mathrm{i}\gamma y_2}\hat{u}_2\left(\mathbf{k}_{13},\omega+k_1\overline{U_1},y_2\right)\frac{\mathrm{d}\overline{U_1}}{\mathrm{d}y_2}\mathrm{d}y_2\\ \hat{p}_{TT}\left(\mathbf{k}_{13},\omega,0\right)=\rho_0\dfrac{d_i d_j}{\mathrm{i}\gamma}\displaystyle\int_0^{+\infty}\mathrm{e}^{\mathrm{i}\gamma y_2}\hat{u}_{ij}\left(\mathbf{k}_{13},\omega+k_1\overline{U_1},y_2\right)\mathrm{d}y_2\end{cases} \tag{72}$$

, where:

$$\begin{cases}\gamma=\sqrt{{k_0}^2-k_{13}^2}\\ \hat{u}_{ij}\left(\mathbf{k}_{13},\omega+k_1\overline{U_1},y_2\right)=\displaystyle\int_{-\infty}^{+\infty}\int_{-\infty}^{+\infty}u_i\left(\mathbf{x}_{13},y_2,t\right)u_j\left(\mathbf{x}_{13},y_2,t\right)\mathrm{e}^{-i\left(\mathbf{k}_{13}\cdot\mathbf{x}_{13}+\omega t\right)}\mathrm{d}\mathbf{x}_{13}\mathrm{d}t\\ (d_1,d_2,d_3)=(k_1,-\gamma,k_3)\end{cases} \tag{73}$$

Substituting Eq.(72) into the relationship Eq.(7) in Section II.A, with calculation and coordinate transformation, we can obtain the expression as follows:

$$\begin{cases}\Phi_{MT}\left(\mathbf{k}_{13},\omega\right)=4\rho_0^2\dfrac{k_1^2}{\gamma^2}\displaystyle\int_{\sigma=0}^{\delta}\mathrm{e}^{\mathrm{i}\left(\gamma-\gamma^*\right)\sigma}\left[\int_{\Delta y_2=-\sigma}^{\sigma}\mathrm{e}^{-\mathrm{i}\frac{\left(\gamma+\gamma^*\right)}{2}\Delta y_2}E_{22}\left(\mathbf{k}_{13},\omega+k_1\overline{U_1},\sigma-\frac{\Delta y_2}{2},\sigma+\frac{\Delta y_2}{2}\right)\mathrm{d}\Delta y_2\right]\left(\frac{\mathrm{d}\overline{U_1'}}{\mathrm{d}\sigma}\right)^2\mathrm{d}\sigma\\ \Phi_{TT}\left(\mathbf{k}_{13},\omega\right)=\rho_0^2\dfrac{d_i d_j d_k^* d_l^*}{\gamma^2}\displaystyle\int_{\sigma=0}^{\delta}\mathrm{e}^{\mathrm{i}\left(\gamma-\gamma^*\right)\sigma}\left[\int_{\Delta y_2=-\sigma}^{\sigma}\mathrm{e}^{-\mathrm{i}\frac{\left(\gamma+\gamma^*\right)}{2}\Delta y_2}S_{ijkl}\left(\mathbf{k}_{13},\omega+k_1\overline{U_1},\sigma-\frac{\Delta y_2}{2},\sigma+\frac{\Delta y_2}{2}\right)\mathrm{d}\Delta y_2\right]\mathrm{d}\sigma\end{cases} \tag{74}$$

Doisy divided the wavenumber domain into acoustic and non-acoustic regions, same with the acoustic component and the hydrodynamic component in Fig. 1. Then, the approach of Von Karman and Pope[55] was employed to transform the velocity tensor into a turbulent kinetic energy for description, and finally obtained the following expression:

$$\Phi\left(\mathbf{k}_{13},\omega\right)=\frac{\rho_0^2 U_\tau^3 e^{+1.5}}{K_+^3}\left[3.5A_1\frac{\mathbf{k}_{13}^2}{K_+^2}H_t\left(K_+\overline{\delta}_i,\overline{\Psi}\right)+\frac{A_2}{e^+}\frac{k_1^2}{\mathbf{k}_{13}^2}H_m\left(K_+\overline{\delta}_i,\overline{\Psi}\right)\right] \tag{75}$$

, where

$$\begin{cases} A_1=30\beta^{4/3};A_2=30\beta^{2/3} \\ H_t\left(X,Y\right)=\int_0^X x^4 e^{-2\frac{Y}{X}x}h_t\left(x\right)\mathrm{d}x \\ H_m\left(X,Y\right)=\int_0^X x^2 D^2\left(\frac{x}{\beta_\delta X}\frac{\overline{\delta}_i}{\delta_i}\right)e^{-2\frac{Y}{X}x}h_m\left(x\right)\mathrm{d}x \\ K_+=\sqrt{\mathbf{k}_{13}^2+\left(\frac{\omega-k_1U_c}{V}\right)^2} \\ \overline{\Psi}=\left|\overline{\mathbf{\Psi}}\right|=\left|\mathbf{k}_{13}\right|\overline{\delta}_i \end{cases} \tag{76}$$

$V\approx U_\tau\sqrt{2e^+}$ is the Kraichnan "sweeping velocity", e^+ is the normalized kinetic energy:

$$\begin{cases} h_m\left(x\right)=\left(\beta^2+x^2\right)^{-\frac{7}{3}} \\ h_t\left(x\right)=\dfrac{\pi\mathrm{B}\left(2,\frac{8}{3}\right)}{4\beta^{\frac{16}{3}}\left[1+0.549\left(x/\beta\right)^2+0.11\left(x/\beta\right)^4+0.045\left(x/\beta\right)^{\frac{14}{3}}\right]} \\ D\left(x\right)=1+\left(\pi x/2\right)\sin\left(\pi x\right) \end{cases} \tag{77}$$

, where $\mathrm{B}\left(x,y\right)$ is the Beta function. In addition, in Eq.(76), the upper limit of the integral $\overline{\delta}_i$ is defined as:

$$\overline{\delta}_i=\begin{cases} \delta_i & \text{for } \left|\Omega_i\right|\le\beta_\omega\delta_i^{+0.75} \\ \delta_i\left(\dfrac{\beta_\omega^4\delta_i^{+3}}{\Omega_i^4}\right) & \text{for } \beta_\omega\delta_i^{+0.75}\le\left|\Omega_i\right|\le\beta_\omega\delta_i^+ \end{cases} \tag{78}$$

, where

$$\delta_i=\frac{\delta}{\beta_\delta},\delta_i^+=\frac{U_\tau\delta_i}{\nu},\Omega_i=\frac{\omega\delta_i}{U_\tau\sqrt{2e^+}} \tag{79}$$

There are four key coefficients in the Doisy model including β, β_δ, e^+ and β_ω. In the original paper by Doisy[14], two sets of coefficients were provided, i.e. 1.5, 4, 2, 0.4 (P. 197 in the reference[14]) and 1, 5, 4.5, 0.4 (P199 in the reference[14]). The authors compared the two sets and found the variables 1.5, 4, 2, and 0.4 to be the best and are thus used in this paper.

III. 1D form of each W-F model

As previously stated, the 1D form of each W-F model in the k_1 direction is also very useful in this field, as in many practical situations, only the W-F spectrum in the streamwise direction are of concern and measured. Note that the 1D form of each W-F model is not simply $\Phi(\mathbf{k}_{13},\omega)$ for a certain value of k_3. Instead, the 1D form of the W-F spectrum is the integral of $\Phi(\mathbf{k}_{13},\omega)$ over the whole range of k_3, written as:

$$\Phi(k_1,\omega)=\int_{-\infty}^{+\infty}\Phi(\mathbf{k}_{13},\omega)dk_3 \tag{80}$$

The authors have attempted to obtain the integration results of Eq.(80) for all the models introduced in section II.C, however, due to the complexity of the expressions it was found that not all the models are analytically integrable. As such, for the integrable models, the analytical integration was conducted whereas for the non-integrable models, a numerical integration method was performed. Details for all are provided below.

A. Analytically integrable models

The analytically integrable models include the Corcos model, the Efimtsov model, the Mellen Elliptical model, the Smol'yakov I model, the Smol'yakov III model and the Chase I model. For example, for the Corcos model, by substituting Eq.(12) into Eq.(80) and analytically calculating Eq.(80), the 1D form of the Corcos model can be obtained as[56]:

$$\Phi(k_1,\omega)=\Phi(\omega)\frac{\alpha_1}{\pi k_c[\alpha_1^{\ 2}+(k_1/k_c-1)^2]} \tag{81}$$

The same can be done to other analytically integrable models. The 1D form of the Efimtsov model is:

$$\Phi(k_1,\omega)=\Phi(\omega)\frac{\Lambda_1}{\pi\left[1+\left(k_1-k_c\right)^2\Lambda_1^2\right]} \tag{82}$$

The 1D form of the Mellen Elliptical model is:

$$\Phi(k_1,\omega)=\Phi(\omega)\frac{\alpha_1}{\pi k_c[\alpha_1^{\ 2}+(k_1/k_c-1)^2]} \tag{83}$$

Note that the 1D form of the Mellen Elliptical model is the same as the Corcos model, therefore in terms of 1D form analysis, it will be omitted.

The 1D form of the Smol'yakov I model is:

$$\Phi(k_1,\omega)=\frac{\Phi(\omega)}{(2\pi k_c)^2}0.974A(\omega)h(\omega)*[f(k_1,\omega)-\Delta f(k_1,\omega)] \tag{84}$$

, where:

$$f(k_1,\omega)=\frac{12.9*k_c^{\ 3}}{k_1^2-2k_1k_c+(1+A^2)k_c^2},\Delta f(k_1,\omega)=\frac{1.985m_1^{\ 3/2}k_c^3}{1.005k_1^2-2.01m_1k_1k_c+(1+A^2)m_1k_c^2} \tag{85}$$

The 1D form of the Smol'yakov III model is:

$$\Phi(k_1,\omega)=\frac{\Phi(\omega)}{2\pi}\{\frac{2h\Lambda_1}{\left[1+\Lambda_1^{\ 2}\left(k_c-k_1\right)^2\right]}-\frac{2(h-1)l_s}{1+l_s^{\ 2}\left(m_1k_c-k_1\right)^2}\} \tag{86}$$

The 1D form of the Chase I model is:

$$\Phi(k_1,\omega)=\frac{2}{3}\rho^2U_\tau^3[\frac{2C_{MT}k_1^2}{K_{MT}^{\ \ 4}}+\frac{C_{TT}\left(2k_1^2+K_{TT}^{\ \ 2}\right)}{K_{TT}^{\ \ 4}}] \tag{87}$$

, where:

$$K_i^{\ 2}=\frac{\left(\omega-U_ck_1\right)^2}{h_i^2U_\tau^{\ 2}}+k_1^{\ 2}+\left(b_i\delta\right)^{-2},i=MT,TT \tag{88}$$

B. Analytically non-integrable models

For analytically non-integrable models, the Simpson integration method was conducted for Eq.(80), i.e.:

$$\int_{-\infty}^{+\infty}\Phi(\mathbf{k}_{13},\omega)dk_3\approx\int_{k_3^b}^{k_3^a}\Phi(\mathbf{k}_{13},\omega)dk_3\approx\frac{h}{3}[f(k_3^a)+f(k_3^b)+4\sum_{i=1}^{n/2}f\left(k_3^{2i-1}\right)+2\sum_{i=1}^{n/2-1}f\left(k_3^{2i}\right)] \tag{89}$$

, where $h=(b-a)/n$ and n is the number of the subintervals and has to be an even number. It can be seen that the limit of the integration has been approximated to be k_3^a and k_3^b instead of infinity, while the value of the two limits requires definition in advance. As such, we tested different integrating ranges and evaluated all analytically non-integrable models to find the best compromise between error and computing cost. For example, the 1D form of the Chase II model was achieved using Eq.(89) with the substitution of Eq.(32), and the upper and lower limits k_3^a and k_3^b were set to be ±20, ±50, ±100, ±400, ±600 and ±800, respectively. The prediction results at different ω are shown in Fig. 3. It can be seen that as the integration range increases, so do the W-F spectra. However, the increase rate dramatically reduces when the limit goes to ±400, ±600 and ±800, and the results of ±600 and ±800 almost overlap. This has been confirmed to occur in all analytically non-integrable models. Consequently, the compromise was set to be ±600.

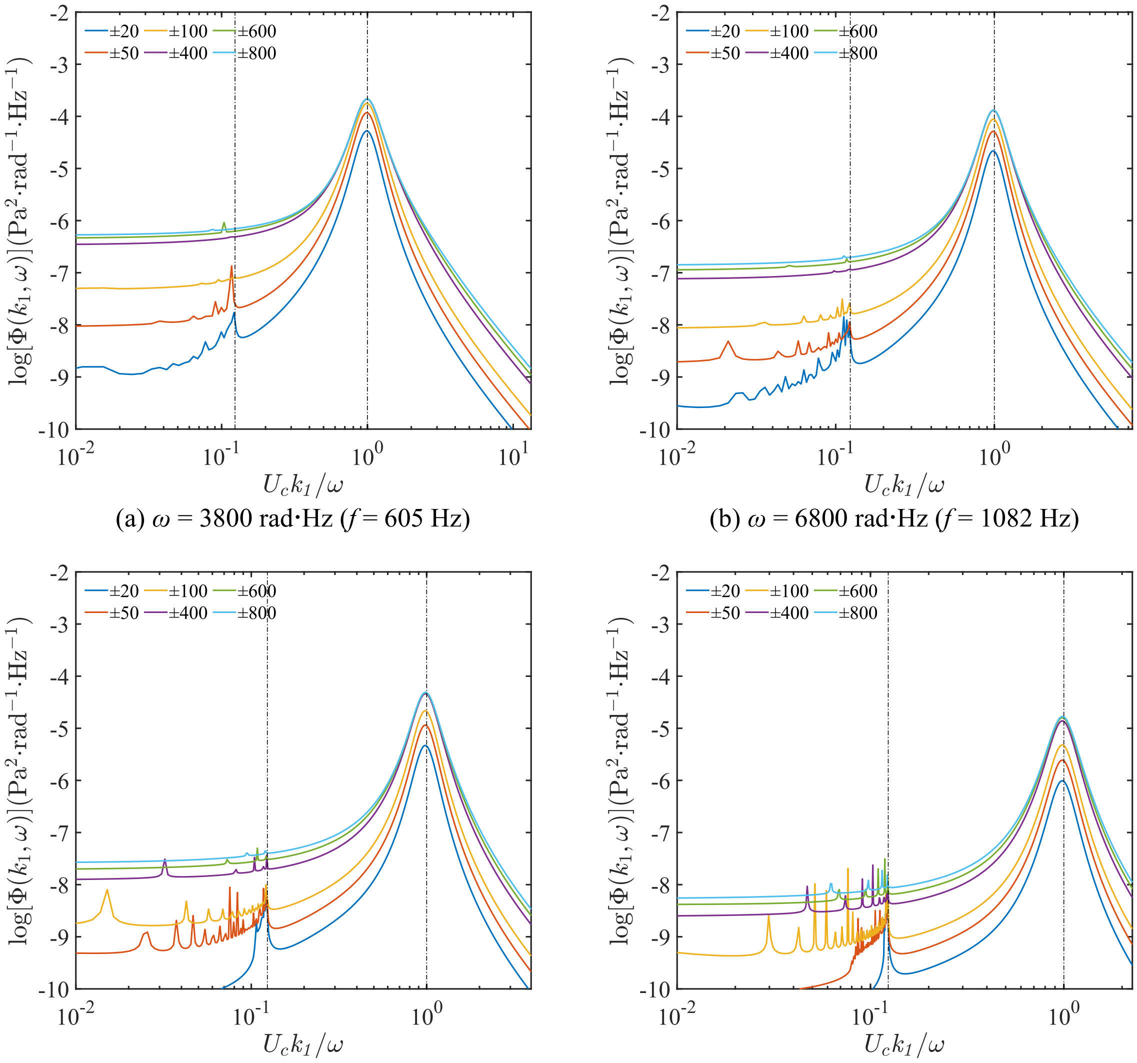

(a) ω = 3800 rad·Hz (f = 605 Hz)　(b) ω = 6800 rad·Hz (f = 1082 Hz)

(c) ω = 12800 rad·Hz (f = 2037 Hz)　(d) ω = 22300 rad·Hz (f = 3549 Hz)

Fig. 3 Comparison of the Chase II model prediction results with different k_1 ranges at different ω

IV. Comparison of the 2D W-F spectra $\Phi(k_1,k_3,\omega)$

A. General parameter settings

In the flat plate TBL-WFPs prediction models mentioned above, the general physical parameters included are freestream velocity U_∞, convection velocity U_c, friction velocity U_τ, speed of sound in the fluid medium c_0, kinematic viscosity v, Reynolds number Re_l, boundary layer thickness δ, boundary layer displacement thickness δ^*, boundary layer momentum thickness θ, and fluid density ρ_0. These are all typical physical parameters in boundary layer theory. By substituting these physical parameters into the model, we can obtain the W-F spectrum and the PSD of the flat plate TBL wall pressure fluctuations under specified operating conditions.

◆Regarding U_∞, three values were used, viz. 30 m/s, 60 m/s, and 90m/s.

◆Regarding c_0, the value was set to be 340 m/s.

◆Regarding v, it was set to be 1.4991×10^{-5} m^2/s.

◆Regarding ρ_0, it is the air density set to be 1.1956kg/m^3.

Due to the great difficulty in measuring the turbulent boundary layer, some physical parameters are difficult to obtain experimentally. Therefore, the following complex physical parameters will be indirectly obtained by substituting known parameters into empirical formulas.

◆Regarding U_c, with the exception of the Smol'yakov III model, which has its own definition, U_c was set to be $0.7U_\infty$ for all models, which is a common approach for TBL studies.

◆Regarding U_τ, it was calculated to be $\sqrt{C_f / (2U_\infty)}$, where C_f is the frictional resistance factor which can be obtained by Schlichting interpolation:

$$C_f = 0.455(\lg Re_l)^{-2.58} \tag{90}$$

For the three Reynolds numbers introduced below, the corresponding U_τ are 1.33 m/s, 2.50 m/s and 3.63 m/s.

◆Regarding $Re_l = U_\infty l/v$, where l is the distance measured from the leading edge of the flat plate in the flow direction. For fully developed turbulence on a smooth flat plate, l is generally taken to be 1 m. The Reynolds numbers corresponding to the three values of U_∞ are 2.0×10^6, 4.0×10^6 and 6.0×10^6.

◆Regarding δ, it was estimated from the empirical formula of the flat plate TBL:

$$\delta = 0.37\frac{l}{Re_l^{1/5}} \tag{91}$$

As such, the corresponding three values of δ are 0.020m, 0.017m and 0.016m.

◆Regarding δ^*, it was approximated to be 1/10 of δ, i.e. 0.1δ.

◆Regarding θ, when Re_l goes to the magnitude order of 10^6, θ is approximately δ/8.

In this paper, 12 models were discussed and compared. As introduced in Section II.B, the Corcos-type models and the non-Corcos-type models have significant differences. The prediction of the W-F spectrum from the six

Corcos-type models first requires a $\Phi(\omega)$ input of TBL-WFP, while the six non-Corcos-type models do not. Regarding the use of the Corcos-type models in practical engineering, generally an empirical model of $\Phi(\omega)$ was input, such as the Chase-Howe model, the Goody model, etc.[57], while experimental data of $\Phi(\omega)$ can be used as the second option. Therefore, the accuracy of the prediction of the Corcos-type model is highly correlated with that of the $\Phi(\omega)$. In contrast, the non-Corcos-type models possess no such correlation and can directly predict the W-F spectrum, so it would be to some extent not reasonable to compare the Corcos-type models with the non-Corcos-type models. As such, the comparison studies were made within the Corcos-type models and within the non-Corcos-type models, respectively. Regarding the Corcos-type models, the Goody model[57] of $\Phi(\omega)$ was used, i.e.:

$$\frac{\Phi(\omega)U_{\infty}}{\tau_w^2\delta}=\frac{C_2(\omega\delta/U_{\infty})^2}{\left[(\omega\delta/U_{\infty})^{0.75}+C_1\right]^{3.7}+\left[C_3(\omega\delta/U_{\infty})\right]^7} \tag{92}$$

, where τ_w is shear stress at the wall, defined as $C_f p_d$, p_d is the dynamic pressure. C_1, C_2, C_3 are model parameters, originally set to 0.5, 3.0, and $1.1R_T^{-0.57}$, respectively, in the reference literature. R_T is defined by the expression $U_\tau^2\delta/U_\infty\nu$.

In this section, we first discuss the comparison of the models of the 2D W-F spectrum. In the next section, the 1D W-F spectrum obtained by integrating the two-dimensional W-F spectrum will be discussed. Note that the general parameter settings are identical.

B. Corcos-type models

A comparison study of each model in 2D form, i.e. $\Phi(k_1,k_3,\omega)$, was conducted using a joint display of the contour plot under the surface plot in Fig. 4, which shows the 2D W-F spectra of the Corcos-type models at different examples of ω when U_∞ =60m/s. Note again that the Goody model is the auto-spectral input for these six Corcos-type models.

To begin with, the overall effects of ω on all models were studied. It can be seen that all models can capture the convective ridge regardless of the shape and amplitude, and when ω increases, the convection ridge moves to higher k_1 with the reduction of the peak amplitude. Moreover, as the angular frequency ω increases, the gradient of amplitude along the spanwise direction weakens. In other words, the amplitude variations along the spanwise direction become less pronounced. Therefore, when ω has a relatively large value, for example ω = 12800 rad·Hz in Fig. 4(c), the choice of the integration range for k_3 has a more significant impact when transitioning from the

2D form to the 1D form. This also confirms previous results, as depicted in Fig. 3, where, among the six different types of integration ranges for k_3, the higher the frequency, as illustrated in Fig. 3(d), the greater the amplitude differences at the convective peak. Conversely, the lower the frequency, illustrated in Fig. 3(a), the smaller the amplitude differences at the convective peak.

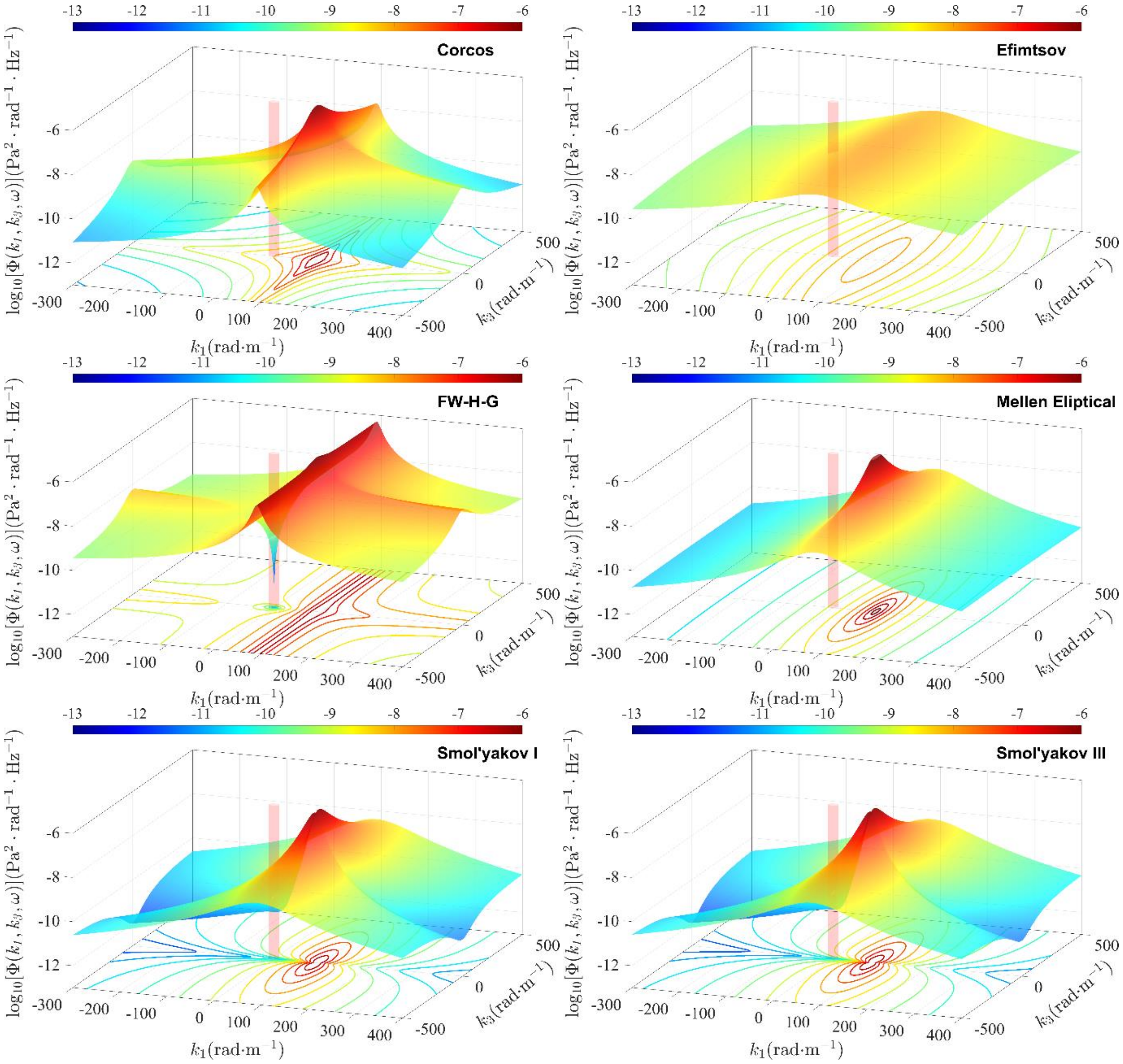

(a) ω = 3800 rad·Hz (f = 605 Hz)

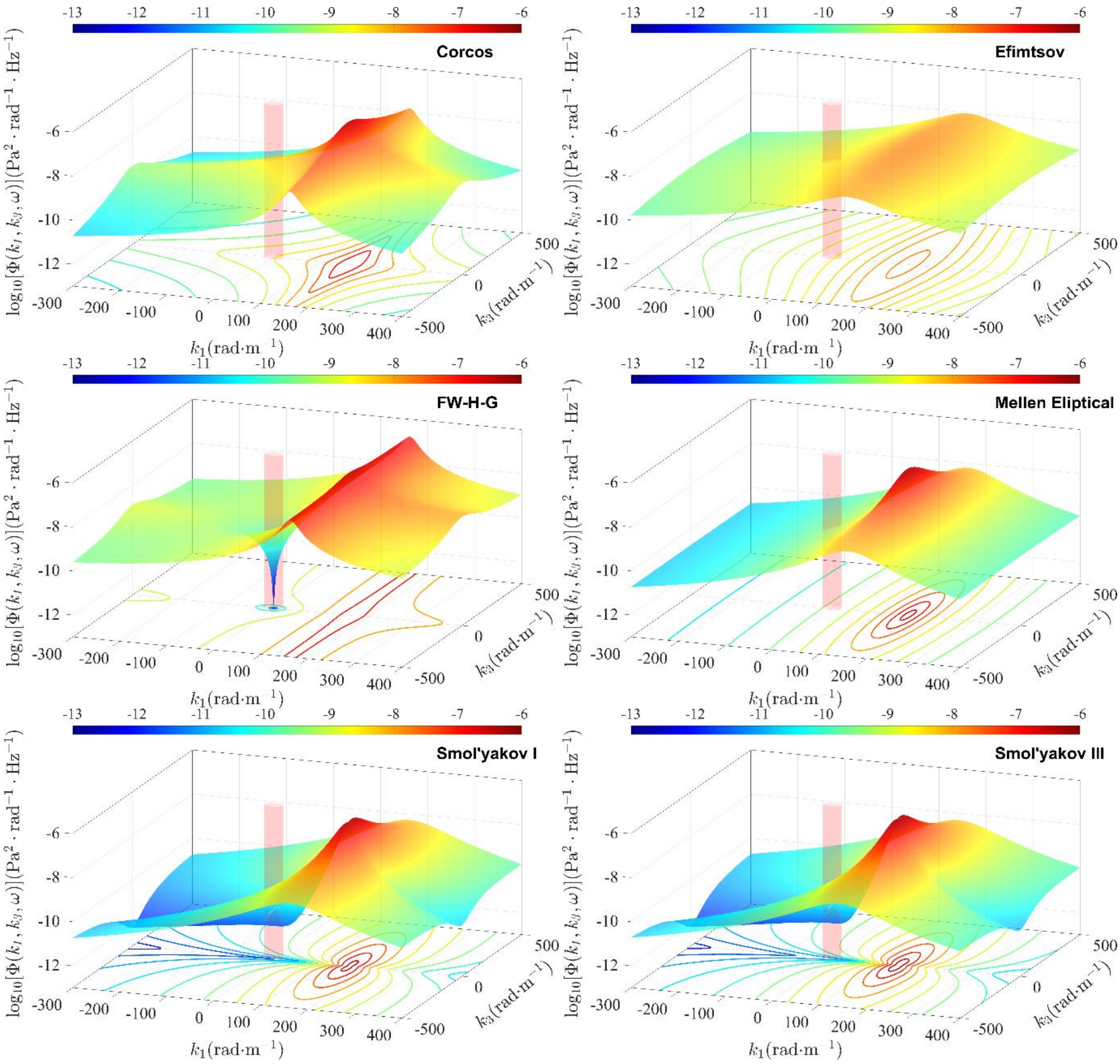

(b) ω = 6800 rad·Hz (f = 1082 Hz)

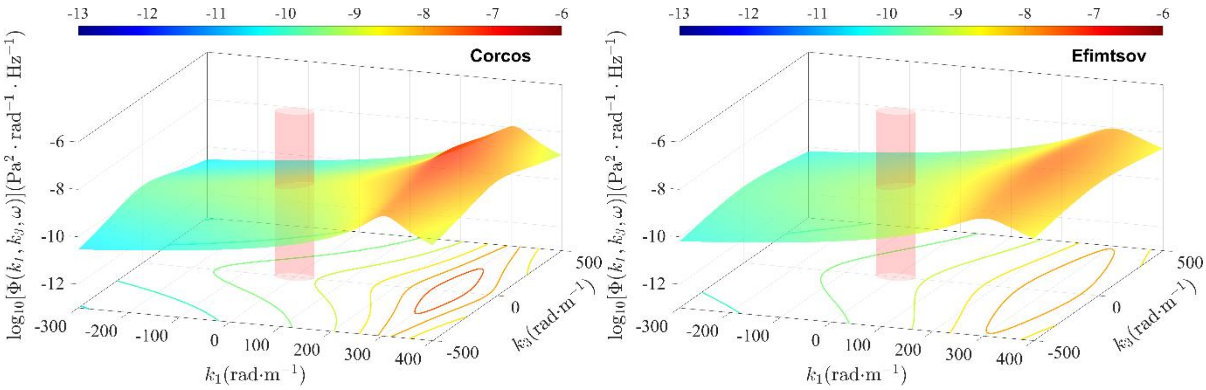

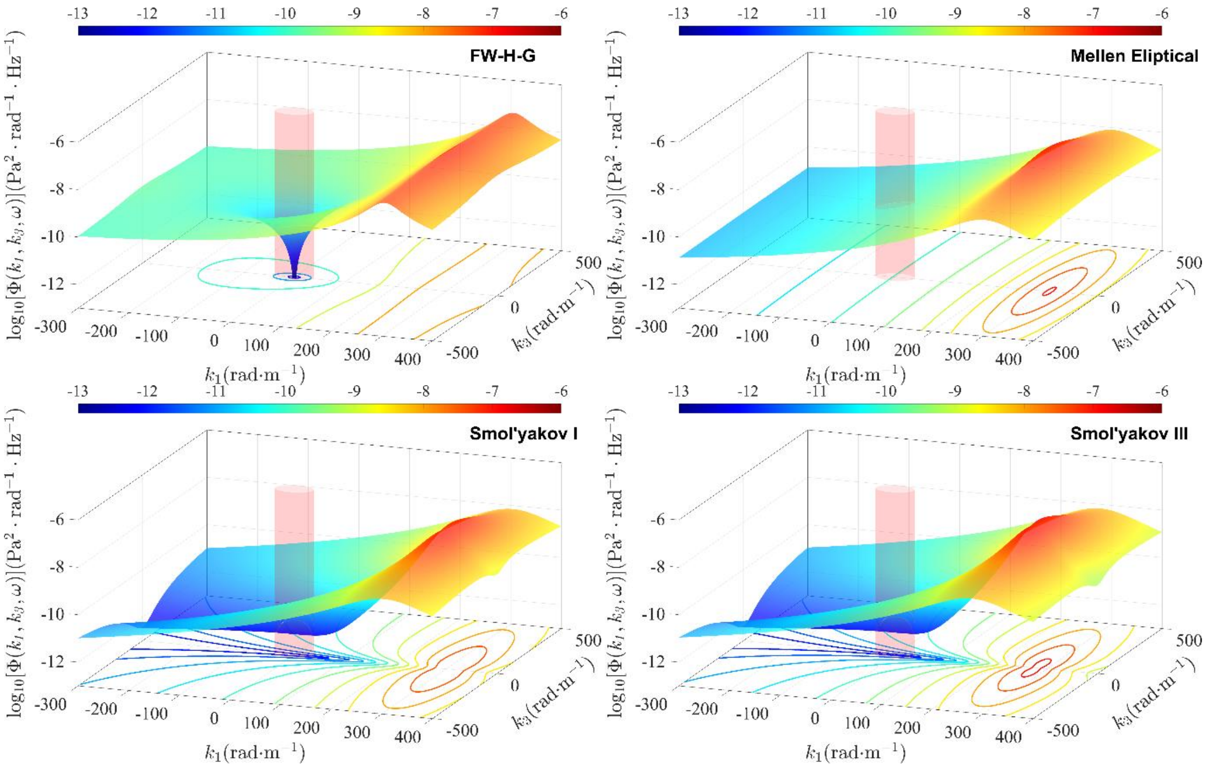

(c) ω = 12800 rad·Hz (f = 2030 Hz)

Fig. 4 2D W-F spectra of the Corcos-type models for different ω, with the red translucent cylindrical surface delineating the boundary of the acoustic region (freestream velocity is 60 m/s)

In addition, the characteristics of different models were studied. At the low frequency ω=3800 rad·Hz, regarding the convective ridge, the six models display different characteristics. First of all, the Efimtsov model is found to be lower than others. Secondly, the Corcos model, the FW-H-G model and the Smol'yakov I\III models all possess four conspicuous ridge lines but with different shapes. More specifically, those of the Corcos and the FW-H-G models in k_1 direction are convex, while those of the Smol'yakov I\III models in k_1 direction are concave. Compared with other models, the FW-H-G model exhibits very small gradients along the convective ridge in the k_3 direction, i.e. it attenuates much less along k_3 direction. Additionally, the FW-H-G model has a noticeable singular point at $\mathbf{k}_{13} = 0$, determined by the term $\left(\mathbf{k}_{13} / k_c\right)^2$ in Eq.(25). As $\mathbf{k}_{13} \rightarrow 0$, the term $\left(\mathbf{k}_{13} / k_c\right)^2 \rightarrow 0$, causes the overall model $\Phi\left(\mathbf{k}_{13}, \omega\right) \rightarrow 0$, thereby forming a singular point at $\mathbf{k}_{13} = 0$. Thirdly, the Smol'yakov I\III models are very similar, which is not just for this frequency but also for all results in this paper. As mentioned in Section II.C, the Smol'yakov III model is distinguished from Smol'yakov I due to four reasons, one of which is the use of an improved model of $\Phi(\omega)$. This is believed to be the most significant reason, so when the same Goody result $\Phi(\omega)$ is used, it will be similar to Smol'yakov I. As for the Mellen Elliptical model, its surface plot is smooth without conspicuous ridgelines, making it stand out and distinguished from other models. At the middle frequency ω=6800 rad·Hz and the high frequency ω=12800 rad·Hz, since the 2D characteristics attenuate, the convective ridge of the models become less conspicuous, and the peak of the convective ridge drastically declines. This corresponds to the energy dissipation of high-frequency small-scale vortices within the boundary layer. Also, the decline of the peak occurs in the Mellen Elliptical model. With these variations, the Corcos, the Efimtsov and the Mellen Elliptical models gradually become very similar.

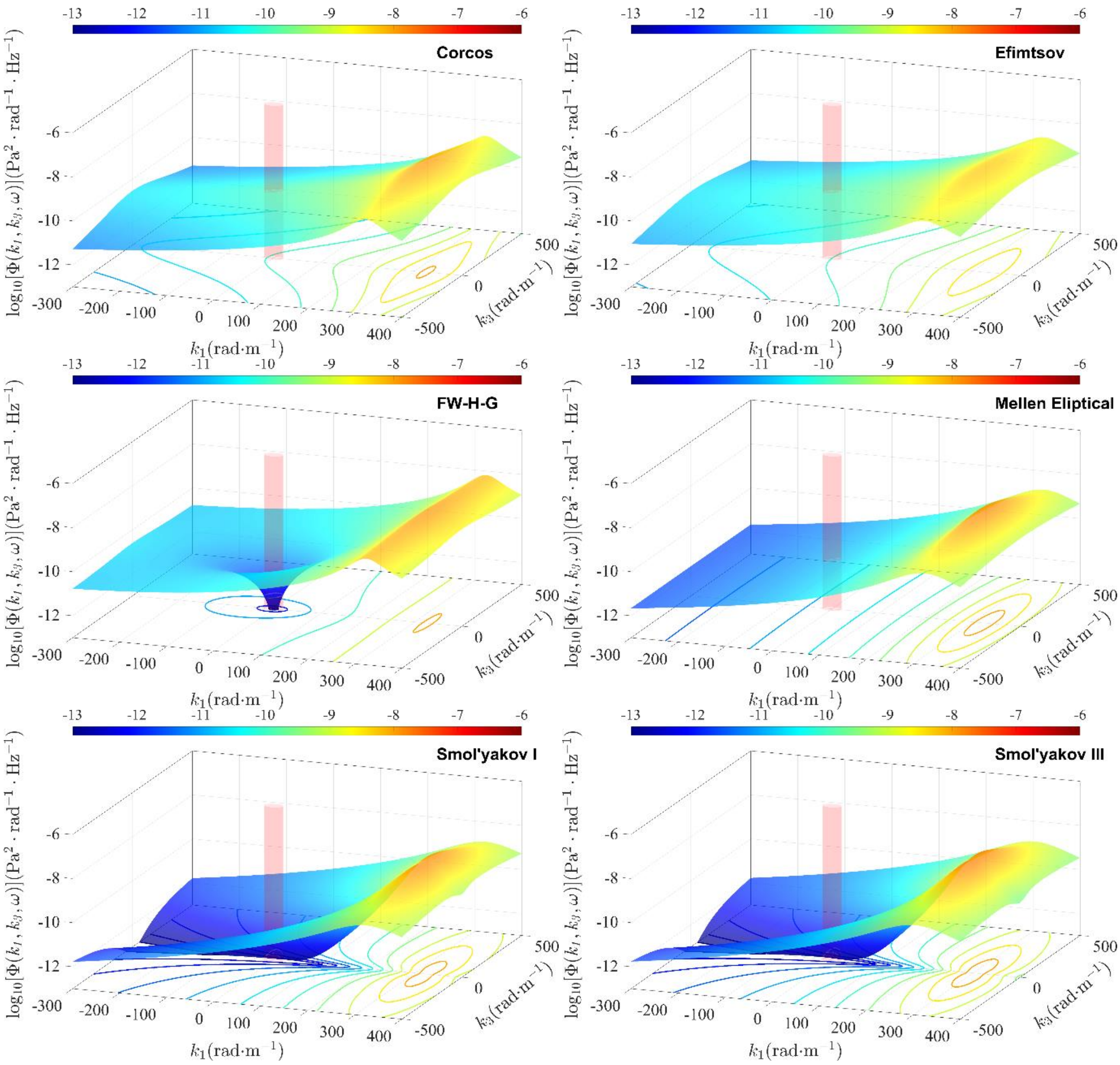

(a) $U_* = 30$ m/s

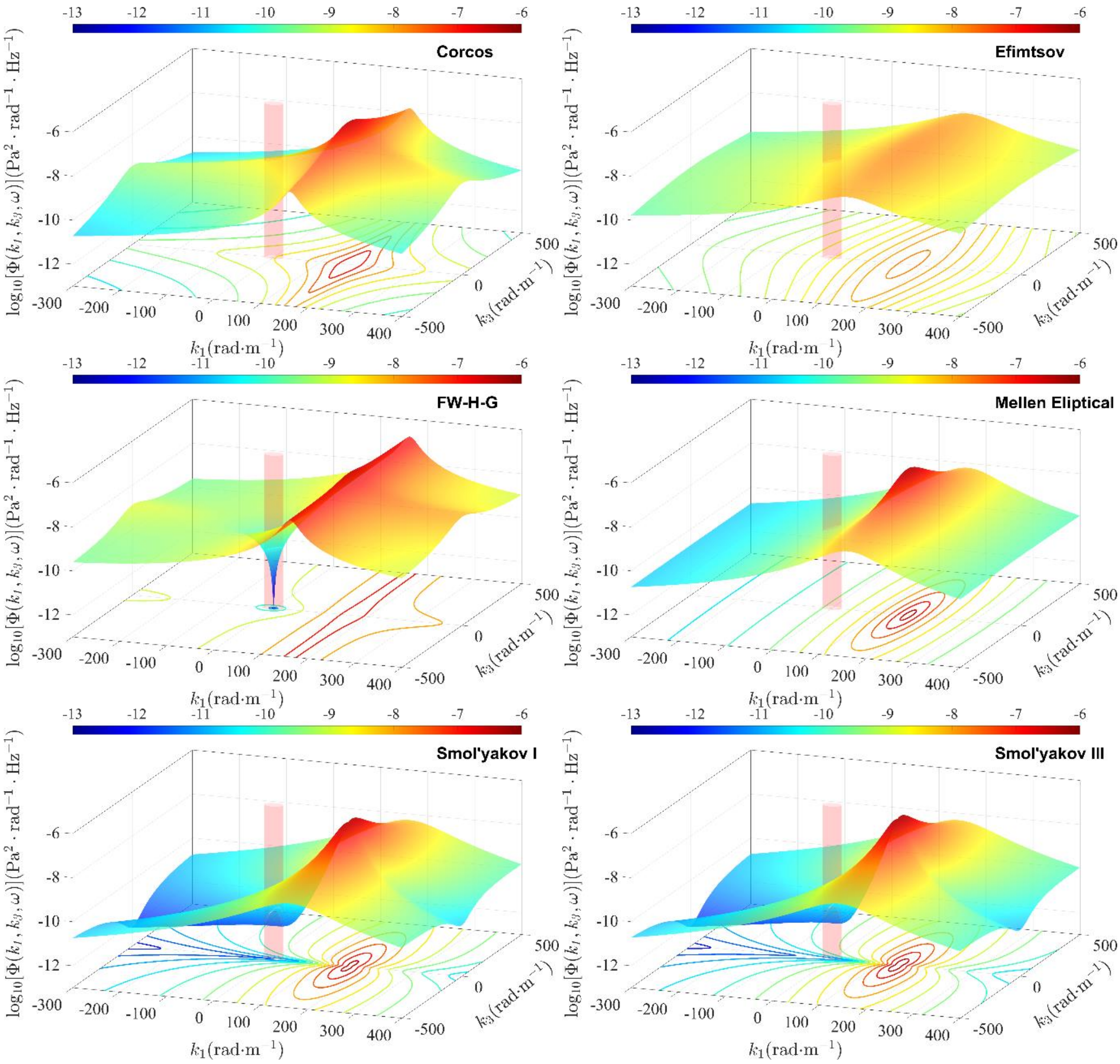

(b) U_∞ = 60 m/s

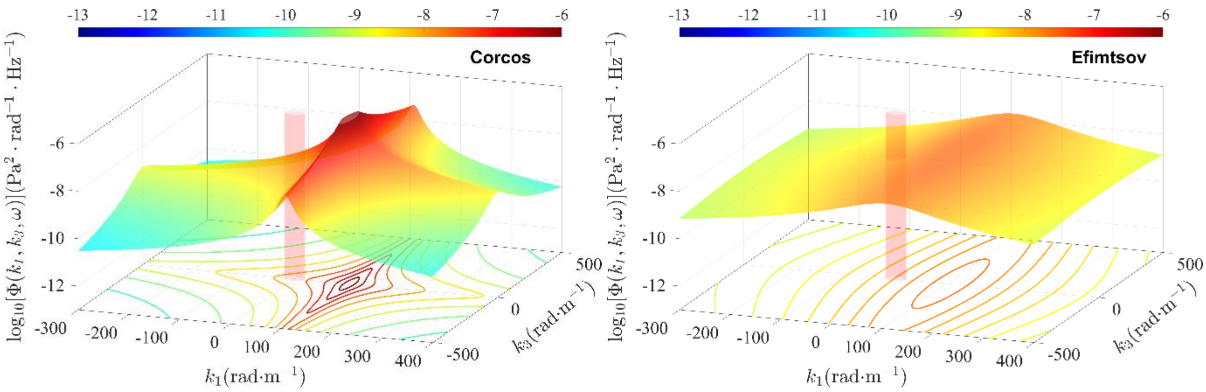

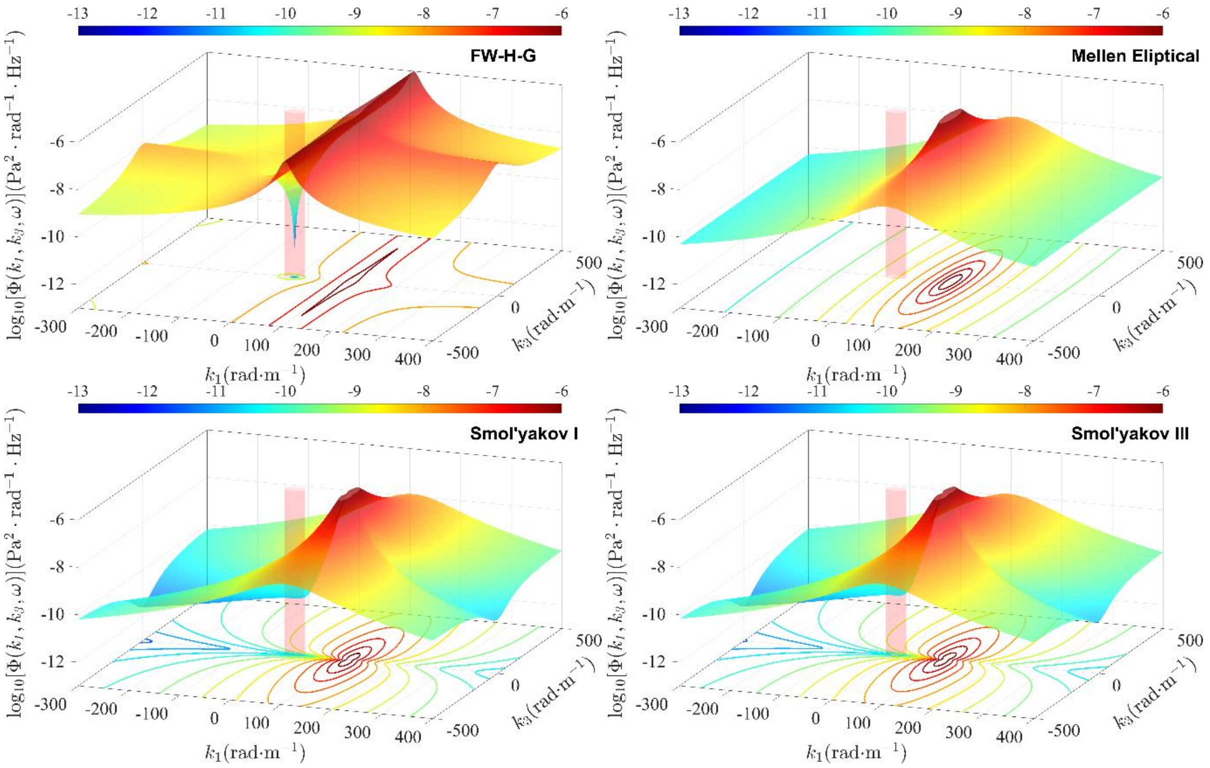

(c) U_∞ = 90 m/s

Fig. 5 2D W-F spectra of the Corcos-type models for different freestream velocity, with the red translucent cylindrical surface delineating the boundary of the acoustic region (ω = 6800 rad·Hz)

The 2D results of Corcos-type models at different freestream velocities U_∞ for a frequency of ω=6800 rad·Hz are shown in Fig. 5. It is evident that for all models, different values for U_∞ alter the position of the convective ridge at the same frequency, while the extent of the acoustic region remains unchanged. Observations indicate that the energy distribution in the k_3 direction varies among different models. For instance, as shown in Fig. 5 (a), (b), and (c), it is evident that with the increase in speed U_∞, the energy distribution of the convective ridge in the k_3 direction becomes more gradual in the Efimtsov model. In other words, the gradient $\partial\Phi/\partial k_3$ of the W-F spectrum in the convective region decreases with increasing speed U_∞. In contrast, the Corcos model, the Mellen Elliptical model, and the Smol'yakov I/III models exhibit an increase in the gradient $\partial\Phi/\partial k_3$ within the convective region as the speed U_∞ increases. Additionally, regardless of the change in speed U_∞, the FW-H-G model maintains a consistently gradual energy distribution in the k_3 direction. Notably, the FW-H-G model displays a singularity at $(k_1, k_3) = (0, 0)$, though it is important to note that this is not an acoustic singularity. This singularity arises due to the term $(\mathbf{k}_{13}/k_c)^2$ in Eq.(25), distinguishing the FW-H-G model from other Corcos-type models. Unlike the Mellen Elliptical model, the Corcos model displays energy-concentrated peaks in both the streamwise and spanwise wavenumbers. However, as mentioned in Section II.B, the 1D form obtained through integration is identical. This indicates that while the energy distribution in the wavenumber domain differs between the 2D W-F spectra of the

Mellen Elliptical model and the Corcos model, their 1D W-F spectra are identical.

C. Non-Corcos-type models

The 2D form of the non-Corcos models has a firm theoretical foundation, including incompressible theory-based models, compressible theory-based models and the Witting model as the only member of the other models in this paper. Likewise, in Fig. 6 the 2D form are compared using a joint display of the contour plot under the surface plot to illustrate the differences in results at different examples of ω.

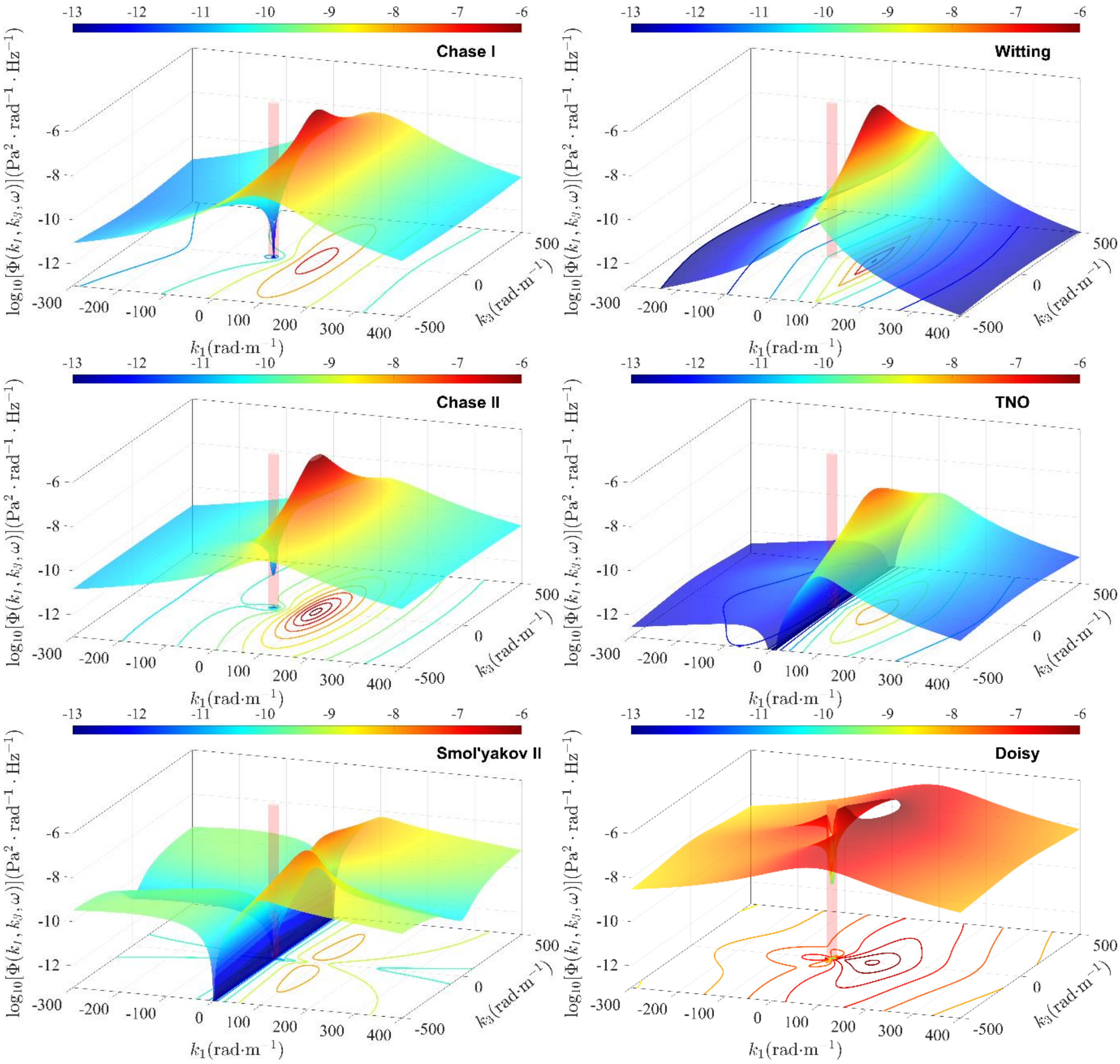

(a) ω = 3800 rad·Hz (f = 605 Hz)

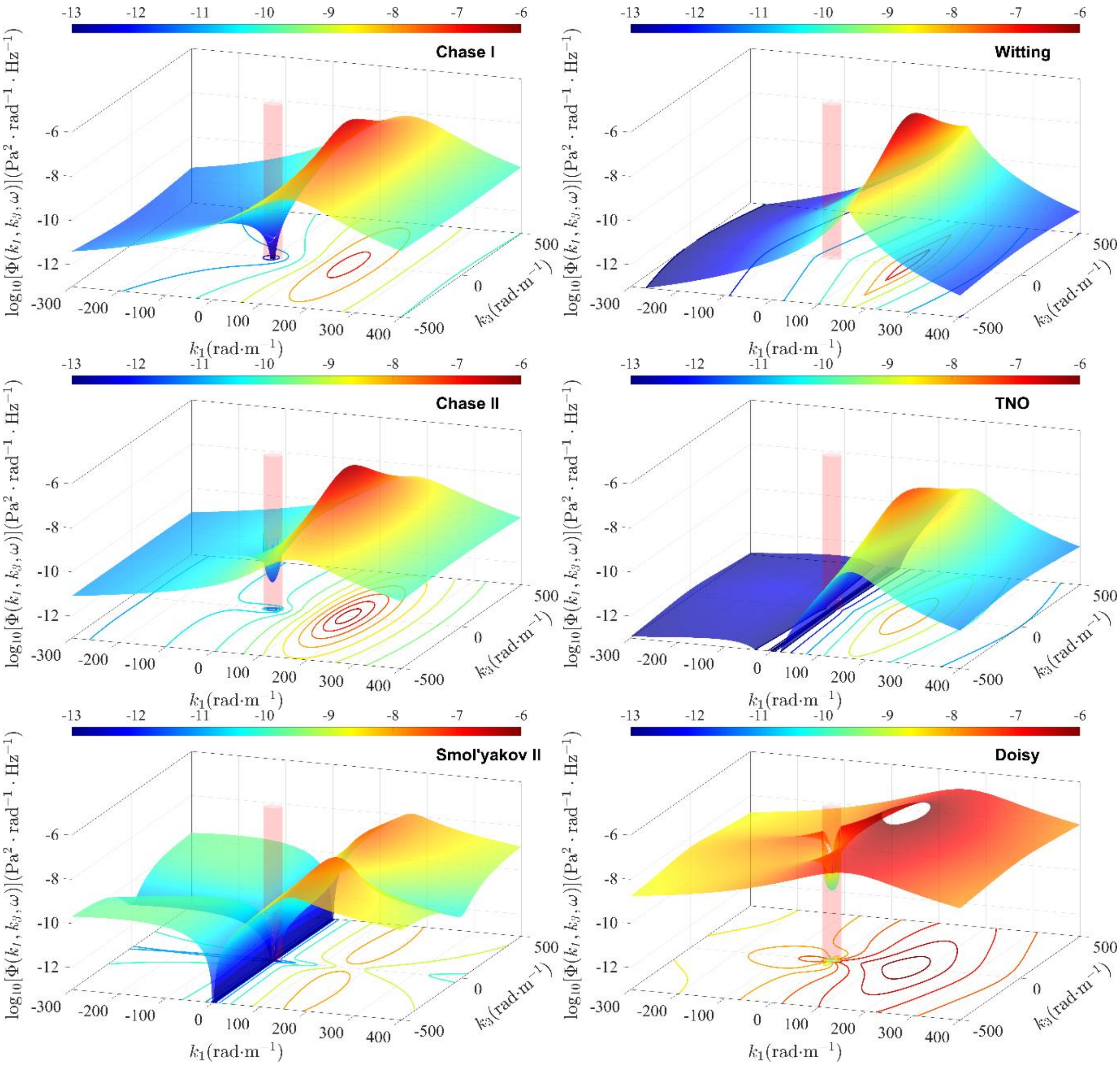

(b) ω = 6800 rad·Hz (f = 1082 Hz)

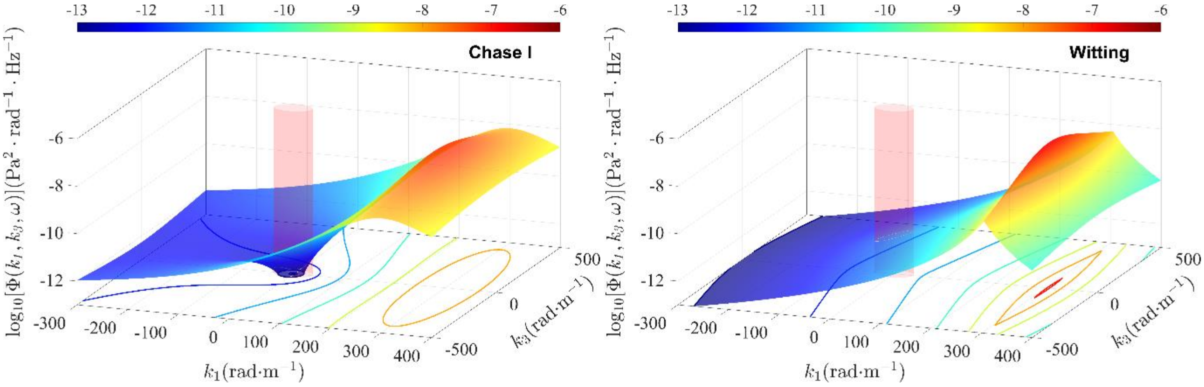

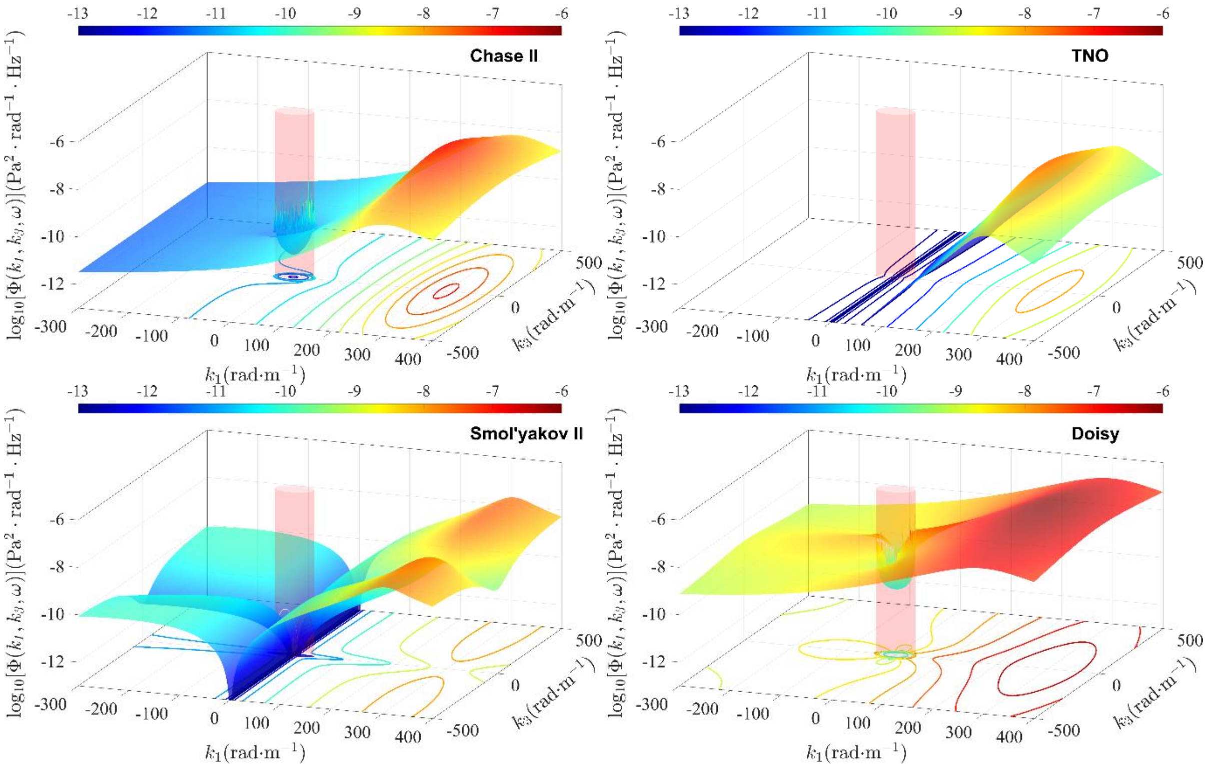

(c) ω = 12800 rad·Hz (f = 2030 Hz)

Fig. 6 2D W-F spectra of the non-Corcos-type models at different ω, with the red translucent cylindrical surface delineating the boundary of the acoustic region (freestream velocity is 60 m/s)

Firstly, like the Corcos-type models, all six models demonstrate the capability of predicting the existence of a convective ridge. The position of these convective ridges shifts in the positive k_1 direction with the increase of ω, accompanied by a decrease in amplitude and a reduction in the correlation with spanwise orientation.

Furthermore, in distinguishing differences among various models, the incompressible theory-based model is derived from the Poisson equation, neglecting the impact of fluid compressibility. The typical Chase I model, TNO model, Witting model, and Smol'yakov II model all fall under the category of incompressible models. It is apparent that the Chase I model has a significant singularity at $\mathbf{k}_{13} = 0$. The amplitude across the entire acoustic region diminishes as $\mathbf{k}_{13} \to 0$, and eventually converges as $\Phi(k_1, k_3) \to 0$. This characteristic resembles that of the FW-H-G model. Consequently, the Chase I model, as an incompressible theoretical model, cannot predict the amplitude in the acoustic region. In comparison to other models, the TNO model is very low in the region where $k_1 < k_0$. Apart from being incompressible, this is also due to the absence of the TT term contribution during the modelling process of the TNO model. From the contour plot, it is observed that the Witting model exhibits a higher gradient in the viscous region compared to any other model. If the Witting model is used for prediction, this may lead to less accurate predictions of the 1D form in the viscous region. The Smol'yakov II exhibits concavity in the k_1 direction and features two convective ridges in the k_3 direction, a characteristic similar to the Smol'yakov I/III models. However, a notable distinction lies in the presence of a clear singularity region at $k_1 = 0$ in the Smol'yakov II model. Additionally, the distance between the two convective ridges increases with frequency.

Finally, we consider the compressible theory-based models, namely, the Chase II model and the Doisy model. To begin with, it can be found that the overall amplitude of the Doisy model is significantly higher than other models. This will probably result in less accuracy of the model but is expected to be corrected. This paper only reviews the original model supplied in the references so we will leave this investigation for future consideration. It is evident that the other four incompressible models exhibit minimal amplitude in the acoustic region where $k_1^2 + k_3^2 < k_0^2$, while the Witting model lacks any distinctive features in the acoustic region. These models do not demonstrate effective predictions in the acoustic region. In comparison to these incompressible models, the Chase II model and the Doisy model exhibit higher amplitudes in the acoustic region. Additionally, both models feature a singular region at the boundary of the acoustic region. Theoretically, this region corresponds to a cylindrical surface defined by $k_1^2 + k_3^2 = k_0^2$, where $\Phi(k_1, k_3, \omega) \to \infty$ as $k_1^2 + k_3^2 \to k_0^2$. However, due to the discretization in numerical results, this singular region may appear as multiple peaks arranged in a circle in the surface plot, as shown in Fig. 6(c). This phenomenon also results in the existence of multiple singular points within the range of $-k_0 < k_1 < k_0$ in the 1D form model. In the case of an integrable model, analytical integration can be used to eliminate this issue.

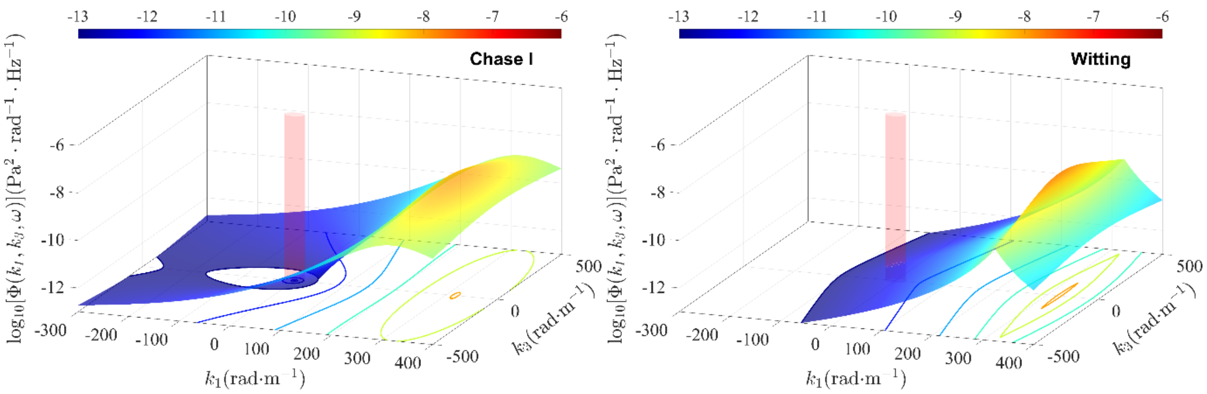

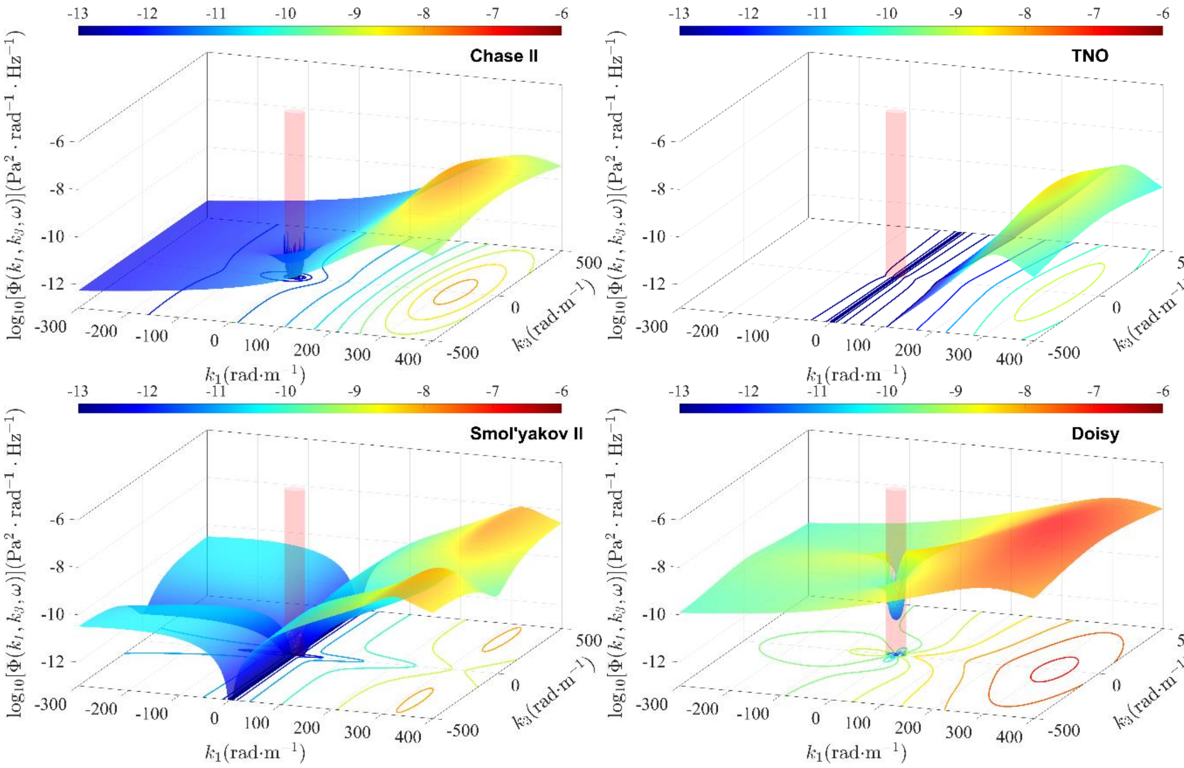

(a) $U_\infty = 30$ m/s

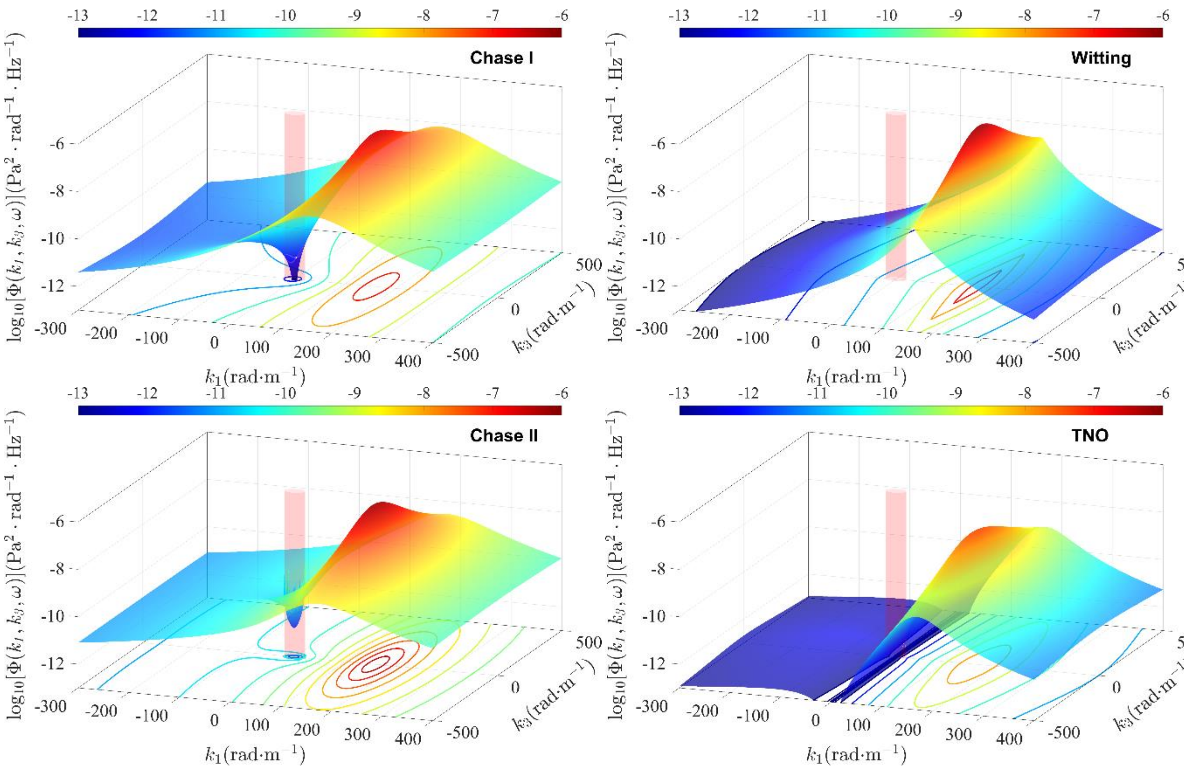

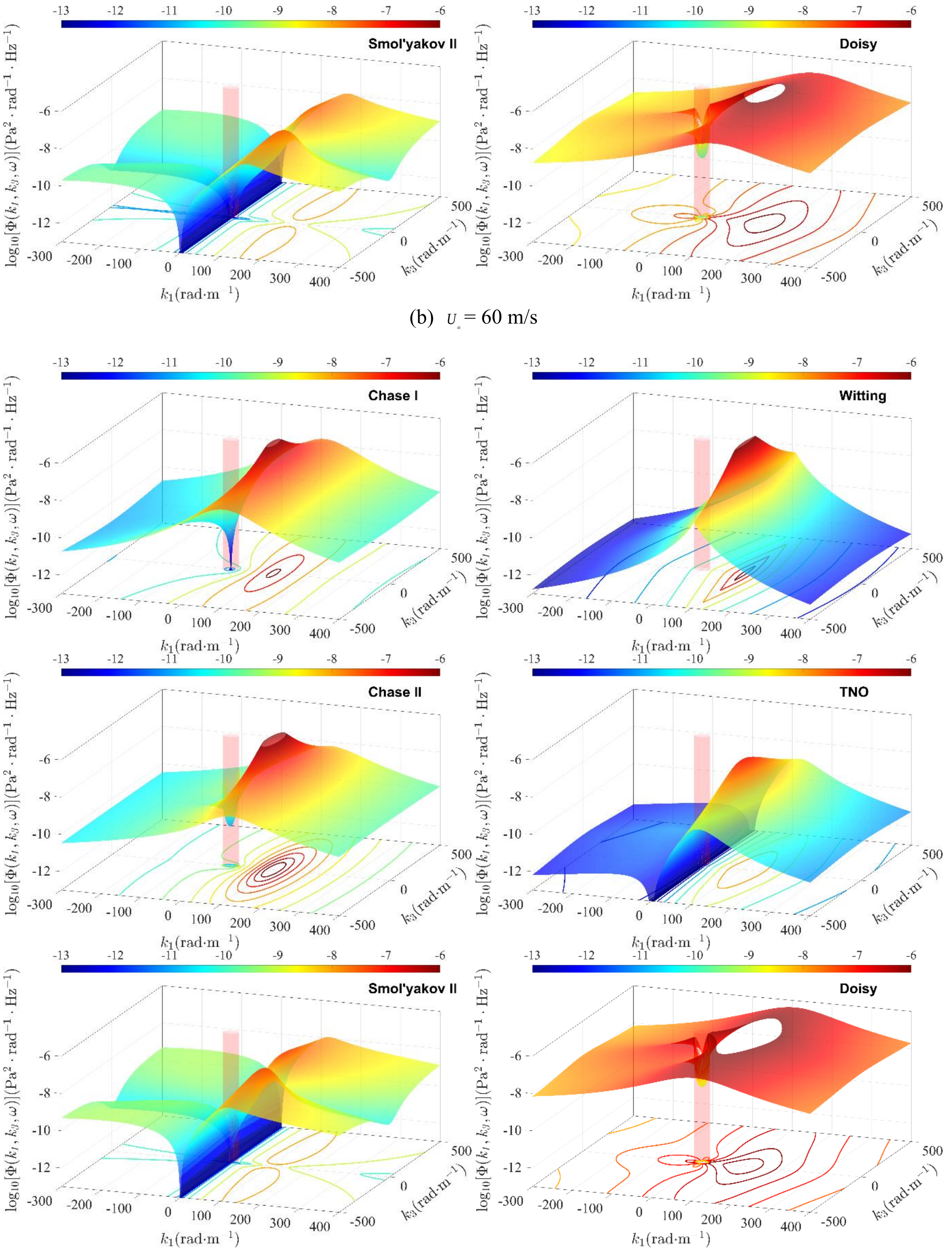

(b) U_∞ = 60 m/s

(c) U_∞ = 90 m/s

Fig. 7 2D W-F spectra of the Non-Corcos-type models for different freestream velocity, with the red translucent cylindrical surface delineateing the boundary of the acoustic region (ω = 6800 rad·Hz)

The 2D results of the non-Corcos models at ω=6800 rad·Hz for different U_∞ are shown in Fig. 7. Similarly, the convection ridge shifts in the negative k_1 direction as the U_∞ increases. In terms of spanwise energy distribution, except for the Smol'yakov II model, the other five models do not depend on the changes in velocity. The Smol'yakov II model exhibits two peaks, and the distribution of these energy peaks becomes more concentrated as the velocity increases. Regarding singularity characteristics, the Chase I model has a singularity that approaches zero at $\mathbf{k}_{13}$=0, while the Smol'yakov II and TNO models exhibit a singular surface at k_1=0. It is noteworthy that the acoustic regions of compressible models such as the Chase II and Doisy models better reflect the compressible characteristics as the Mach number increases. Since the frequency in the figure is the same, the range of the acoustic region is consistent for all velocities. It is clearly evident from the figure that as the velocity increases, the amplitude within the acoustic region of the two compressible models, i.e. the Doisy model and the Chase II model, also increases correspondingly. Additionally, unlike incompressible models with acoustic region characteristics, compressible models can exhibit characteristics of the acoustic region.

V. Comparison of the 1D W-F spectra $\Phi(k_1,\omega)$

A. Corcos-type models

Fig. 8 presents a comparison of the 1D W-F spectral models for different values of ω. As previously mentioned, the 1-D form of the Mellen Elliptical model is identical to the Corcos model, thus it has been omitted from the analysis. Additionally, two vertical lines have been added to indicate the positions of $U_c k_0/\omega$ and $U_c k_c/\omega$, which mark the boundaries of the acoustic region and the theoretical location of the convective ridge peak, respectively.

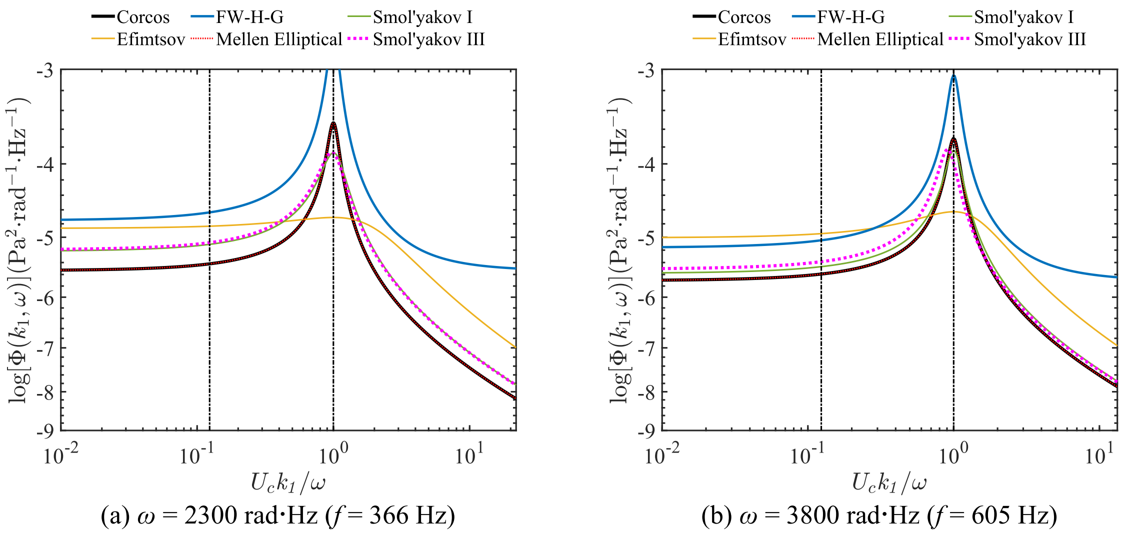

(a) ω = 2300 rad·Hz (f = 366 Hz) (b) ω = 3800 rad·Hz (f = 605 Hz)

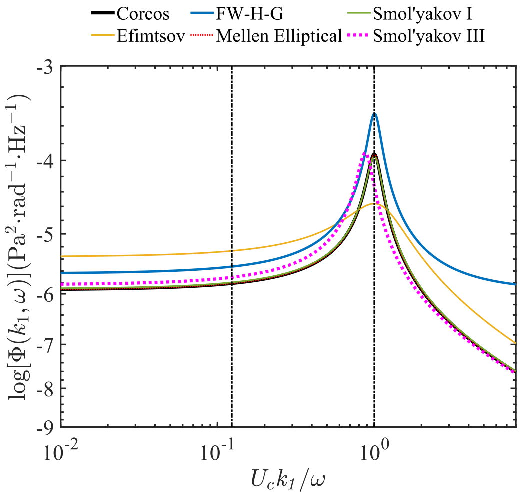

(c) ω = 6300 rad·Hz (f = 1003 Hz)

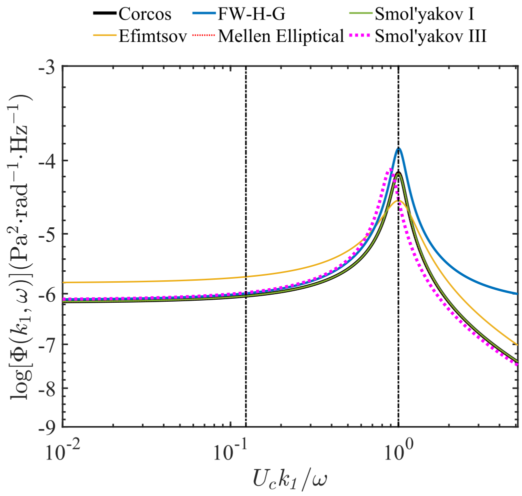

(d) ω = 9800 rad·Hz(f = 1560 Hz)

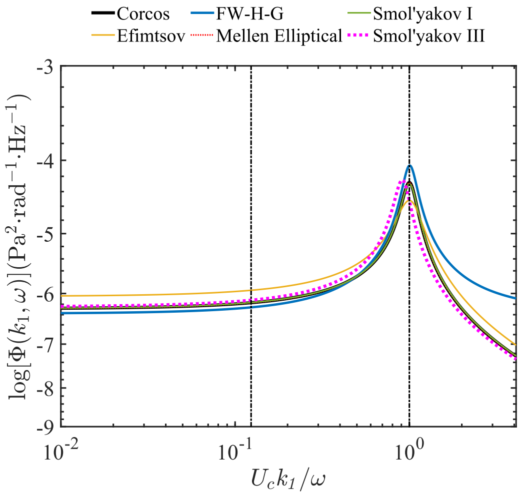

(e) ω = 12300 rad·Hz (f = 1958 Hz)

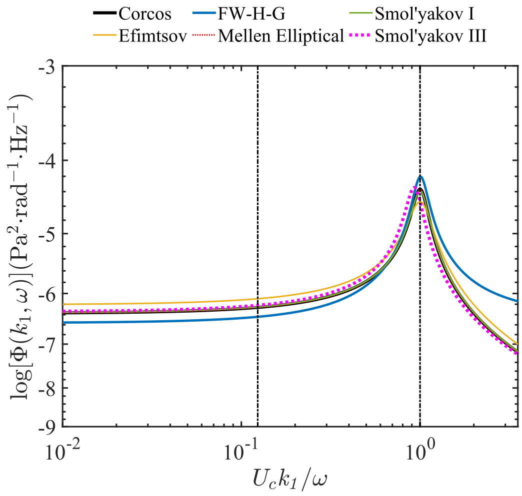

(f) ω = 14300 rad·Hz (f = 2276 Hz)

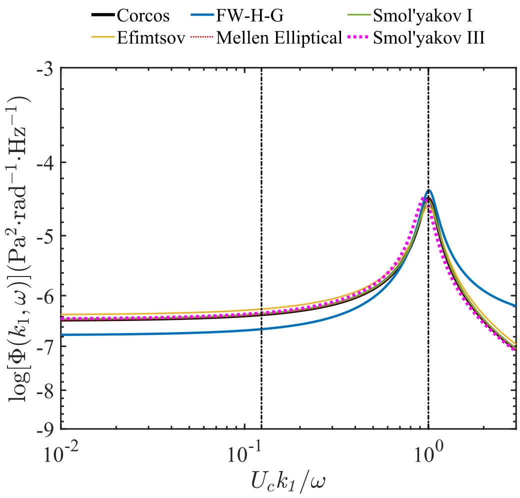

(g) ω = 16800 rad·Hz (f = 2674 Hz)

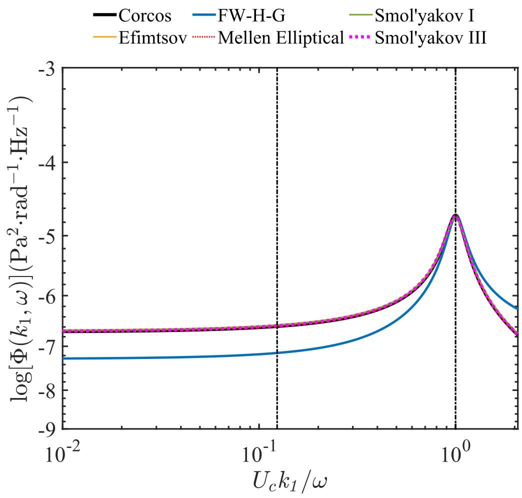

(h) ω = 24300 rad·Hz (f = 3867 Hz)

Fig. 8 1D W-F spectra of the Corcos-type models at different ω, with the two vertical lines representing the boundaries of the acoustic region (left) and the theoretical position of the convective ridge peak (right), respectively (U_∞=60 m/s)

Conclusions can be drawn from Fig. 8 that, under different conditions of ω and k_1, Corcos-type models exhibit significant differences. The analysis is anchored on the Corcos model, as the remaining five models are variants based on the Corcos model. On one hand, across the entire frequency spectrum, the Corcos model shows lower magnitudes in both the acoustic and viscous regions at low frequencies (ω < 6300 rad·Hz), whereas within the intermediate (9800 rad·Hz < ω < 14300 rad·Hz) and high-frequency (ω > 16800 rad·Hz) regimes, its magnitudes gradually exceed those of the FW-H-G model. On the other hand, as the frequency increases, the Corcos model progressively aligns with the Smol'yakov model.

As illustrated in Fig. 8(a) ~(b) about ω = 2300 rad·Hz and ω = 3800 rad·Hz, within the low-frequency range, the convective ridge peak characteristics of the Efimtsov model are notably weaker compared to the other five Corcos-type models. More specifically, the predictive performance of the Efimtsov model regarding the convective ridge is less satisfactory in the low-frequency region, which may be attributed to the strong frequency dependence of parameters Λ_1 and Λ_3 in Eq.(22). As depicted in Fig. 8 (a)~ (d), within the low and mid-frequency ranges, the Efimtsov model exhibits an amplitude in the subconvective region and acoustic region that exceeds those of the other models by an order of magnitude. This may be attributed to its consideration of boundary layer thickness, which plays a more important role within the low-frequency range [19]. As ω increases, the Efimtsov model gradually begins to converge with the Corcos model.

The FW-H-G model is shown, when ω is $\leq$ 6300 rad·Hz, to be higher than any other models in terms of the convective region and the viscous region. This has been explained from the 2D W-F spectrum in Section IV.B, i.e. the FW-H-G model attenuates less than others in the k_3 direction, and the 1D result is from the integration along the k_3 direction. However, the difference declines as ω increases, and as ω is >6300 rad·Hz, the two regions go lower in difference scale. More specifically, the convective region becomes roughly the same as the other models, while the viscous region consistently remains elevated. This discrepancy arises from the FW-H-G model inclusion of the $(\mathbf{k}_{13}/k_c)^2$ term, as shown in Eq.(25), which is absent in the typical Corcos model. Consequently, as k_1 increases into the viscous region, the amplitude correspondingly intensifies. Therefore, across the entire frequency range, the FW-H-G model exhibits relatively higher magnitudes in the viscous region. In the acoustic and subconvective regions, the amplitude of the FW-H-G model varies significantly with frequency. As shown in Fig. 8(a), it exhibits higher amplitude compared to the other models, except for the Efimtsov model. However, as the frequency increases, i.e. ω = 16800 rad·Hz and ω = 24300 rad·Hz in Fig. 8 (g) and (h), the amplitude in the acoustic region becomes lower than that of all the other models.

The Smol'yakov I and III models exhibit lower convective ridge peaks compared to the Corcos model at ω =2300 rad • Hz. However, as the frequency increases, the results of the Smol'yakov I and III models become almost identical to those of the Corcos model. When comparing the two Smol'yakov models, they may appear to overlap without close examination, with the primary differences manifesting at the convective ridge peak. As previously noted, Smol'yakov posits that U_c is dependent of ω and approximates U_c using his unique equation, Eq.(67), which seems to enhance the prediction of the convective ridge peak location.

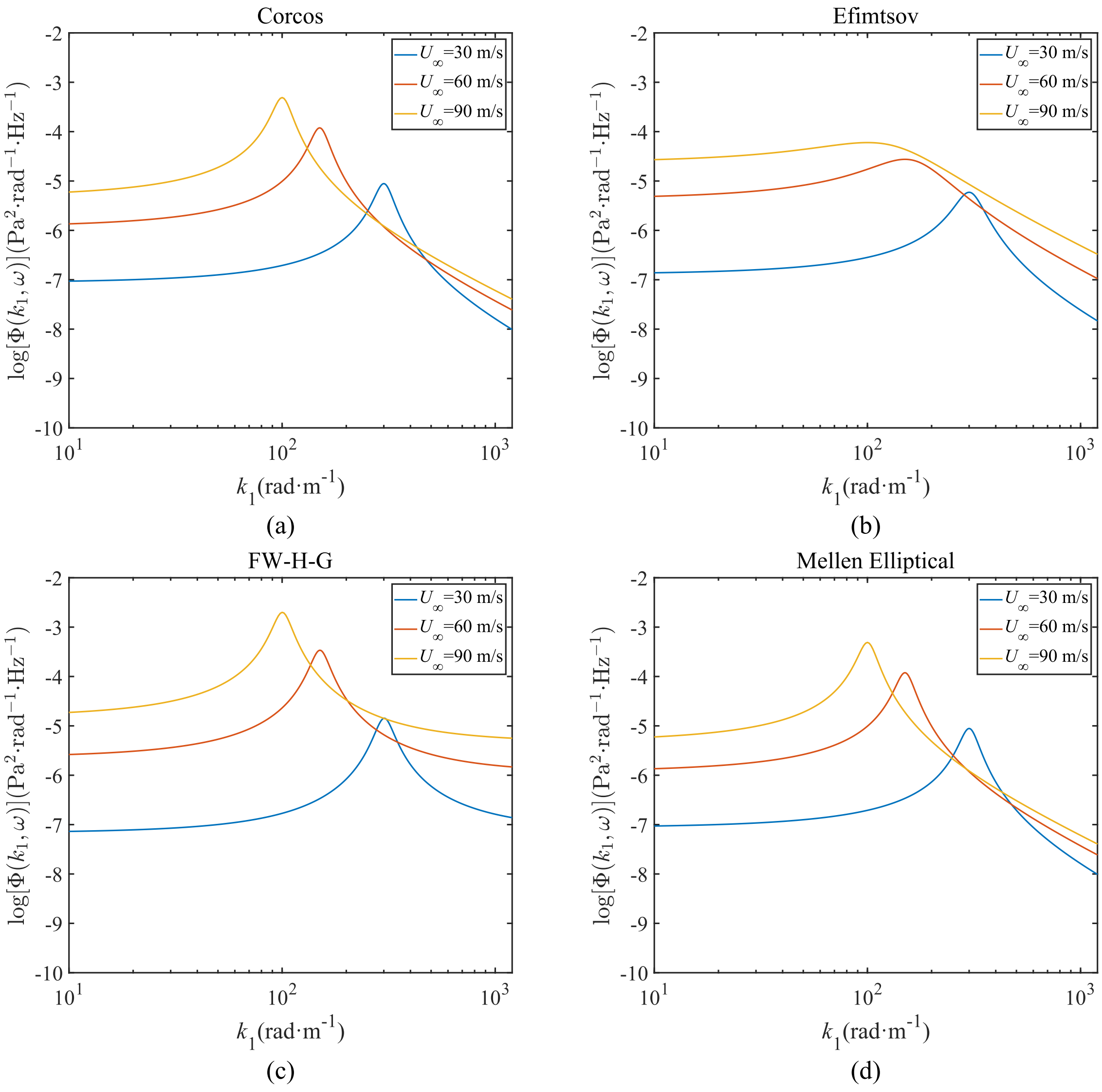

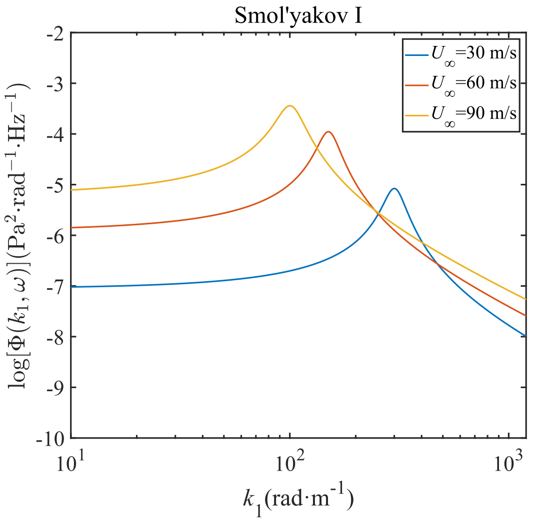

(e)

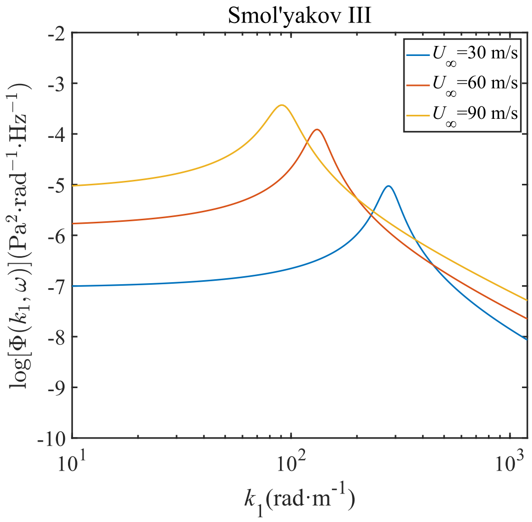

(f)

Fig. 9 1D W-F spectra of the Corcos-type models at different U_∞ (ω = 6300 rad·Hz)

Fig. 9 compares the 1D W-F spectral results for Corcos-type models at the same frequency ω=6300 rad·Hz under different velocities. In this figure, the Efimtsov model exhibits a pronounced convection ridge peak at U_∞=30m/s, but this peak is much weaker at U_∞=90m/s. From Fig. 9 (c), it can be observed that as U_∞ increases, the high-wavenumber viscous region also rises, and this upward trend is higher than in other models. As previously mentioned, the 1D form of the Corcos model is identical to that of the Elliptical model. Similarly, the Smol'yakov I and Smol'yakov III models are also largely similar.

B. Non-Corcos-type models

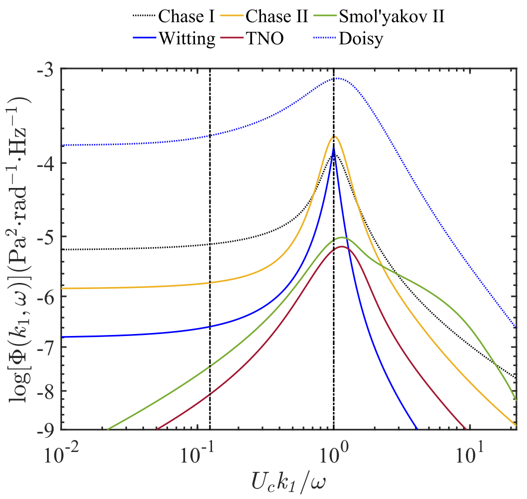

(a) ω = 2300 rad·Hz (f = 366 Hz)

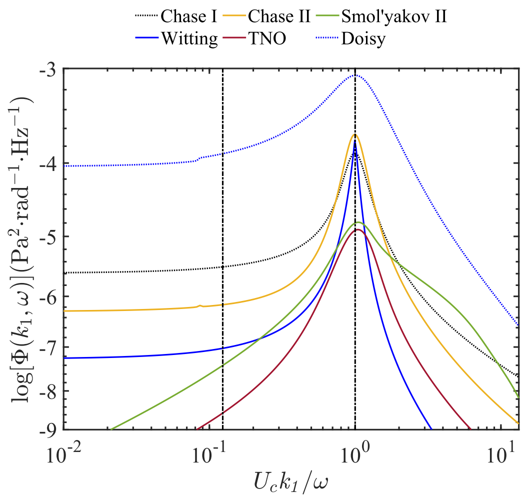

(b) ω = 3800 rad·Hz (f = 605 Hz)

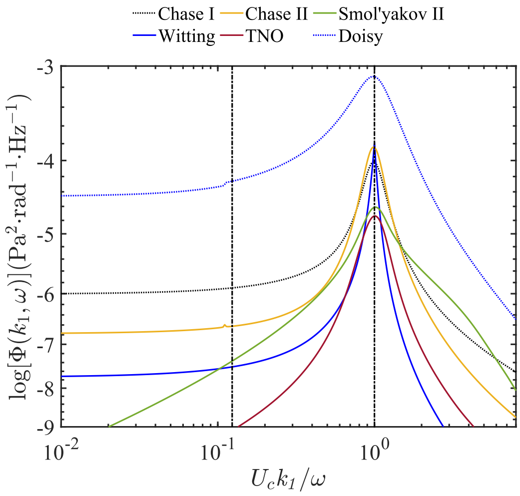

(c) ω = 6300 rad·Hz (f = 1003 Hz)

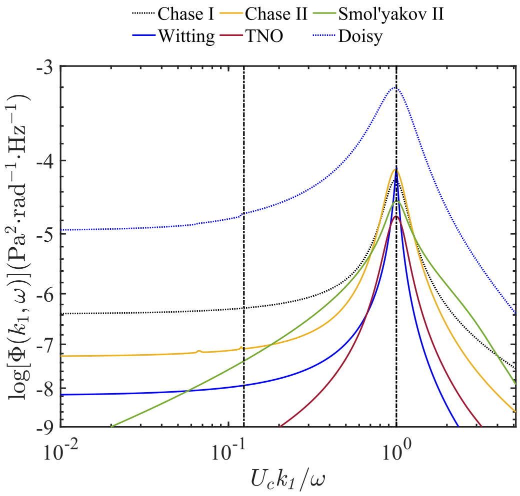

(d) ω = 9800 rad·Hz (f = 1560 Hz)

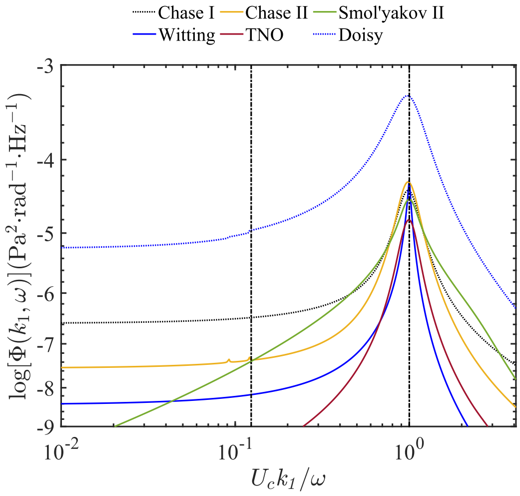

(e) ω = 12300 rad·Hz (f = 1958 Hz)

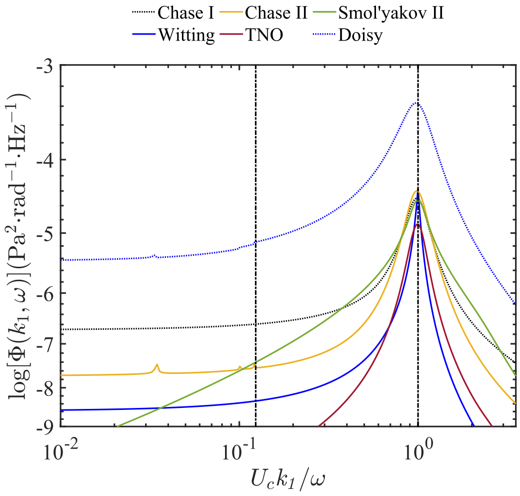

(f) ω = 14300 rad·Hz (f = 2276 Hz)

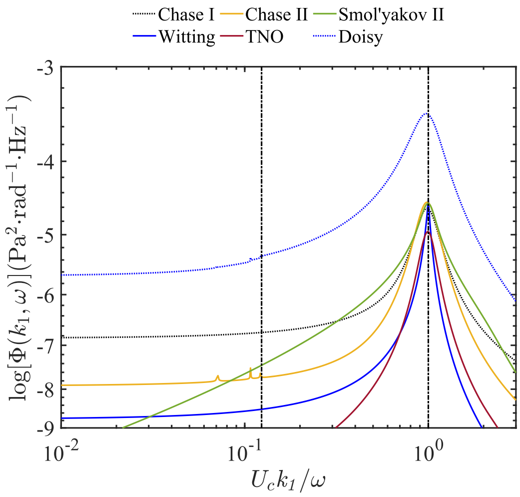

(g) ω = 16800 rad·Hz (f = 2674 Hz)

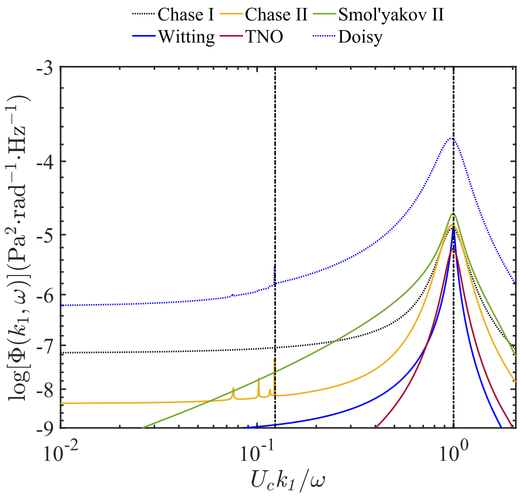

(h) ω = 24300 rad·Hz (f = 3867 Hz)

Fig. 10 1D W-F spectra of the non-Corcos-type models at different ω, with the two vertical lines representing the boundaries of the acoustic region (left) and the theoretical position of the convective ridge peak (right), respectively(U_∞ =60 m/s)

First, we begin the analysis with the acoustic region. Compared to Corcos-type models, the differences among non-Corcos-type models are quite pronounced. Notably, because the Smol'yakov II and TNO models consider only the MT term while neglecting the TT term, this directly results in the predicted $\Phi(\mathbf{k}_{13},\omega)$ in the acoustic region displaying a dependence on $k_{13}{}^2$, i.e. the Kraichnan-Phillips theory previously mentioned. As noted in Section IV.C, the 2D W-F spectra of the Chase II and Doisy models exhibit singularities on the $k_1^2+k_3^2=k_0^2$ acoustic wavenumber boundary surface. Since the 1D wavenumber spectrum requires integration over k_3, this integration passes through this circular region, and numerical discretization further complicates the process, resulting in multiple singularities within the acoustic region. From Fig. 10, it can be observed that as ω increases, the peak amplitude within the acoustic region boundary of the Chase II model gradually grows larger, making the singularities within the acoustic region more prominent. The primary reason is that numerical integration cannot accurately predict singularities due to discretization.

Furthermore, the convective region is a critical aspect of the 1D wavenumber spectrum, as the shape of the convective ridge directly reflects the predictive accuracy in the subconvective and viscous regions. In terms of the width of the convective ridge, the Witting model is the narrowest, followed by the TNO model, while the Doisy model narrows as the frequency increases. The magnitude of the convective ridge peak is also an important characteristic of the convective region. At $\omega = 2300\ \mathrm{rad\cdot Hz}$, as shown in Fig. 10(a), the peak magnitudes in descending order are: the Doisy model, Chase II model, Witting model, Chase I model, Smol'yakov II model, and TNO model. As the frequency increases, the peak values of all models, except the Doisy model, converge.

Overall, the omission of the TT term results in poorer performance of the TNO model and Smol'yakov II model in the subconvective region. Inclusion of the TT term for correction may improve the predictive performance. Both the Chase II and Doisy models capture the compressibility features of the fluid, with the Doisy model, as a representative of compressible models, showing an increase by a factor of 10 compared to the other models. However, it is believed that its four model parameters (β, β_δ, e^+, β_ω) offer considerable flexibility and potential for improvement. By adjusting these parameters, further refinement in predictions can be expected.

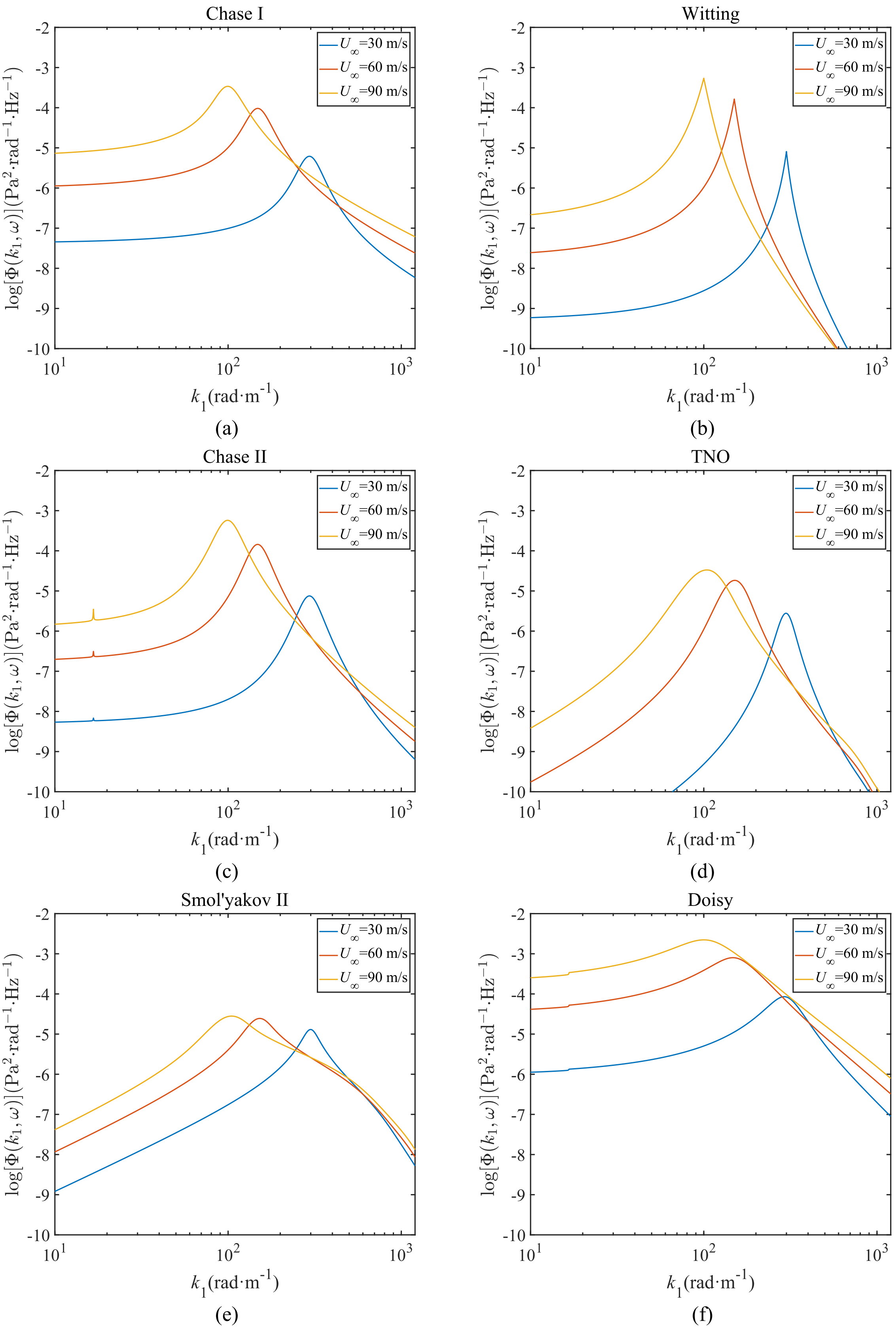

Fig. 11 1D W-F spectra of the non-Corcos-type models at different U_∞ (ω = 6300 rad·Hz)

The 1D results of the non-Corcos models are shown in Fig. 11. Focusing first on the high-wavenumber viscous region, Fig. 11 (d)~ (e) show that the amplitude within the viscous region for the TNO and Smol'yakov II models does not vary significantly with changes in the incoming flow velocity U_∞. The viscous regions of the Chase I, Chase II, and Doisy models increase with increasing U_∞. However, the viscous region of the Witting model decreases with increasing U_∞. Observing the acoustic region, the Chase II model exhibits a distinct singularity at the boundary of the acoustic region, which becomes more pronounced with increasing U_∞. Similarly, another compressible model, the Doisy model, also shows a distinct discontinuity singularity in the acoustic region.

VI. Conclusions

This paper conducted a systematic review of twelve TBL-WPFs W-F spectrum models in both 2D and 1D forms. These models were classified into two categories according to whether the models require a $\Phi(\omega)$ input of TBL-WPFs, i.e. Corcos-type models and Non-Corcos-type models. Due to differences in the theoretical foundation, the latter category was furthermore subdivided into the incompressible theory-based models, the compressible theory-based models, and the others. The review provided a brief introduction into each model, including their modelling approach and their final 2D form expression of $\Phi(\mathbf{k}_{13},\omega)$. To achieve the 1D form of each model, integration of the 2D form along the full range of k_3 were conducted. However, not all these models can be analytically integrated along k_3, so those models are also subdivided into analytically integrable models and analytically non-integrable models, the numerical integration method has been used for the latter type. To facilitate comparison of those models, identical general parameters were set for all the models, such as U_∞ and c_0. The comparison was made among the Corcos-type models and Non-Corcos-type models, respectively. Regarding the Corcos-type models, the input of $\Phi(\omega)$ was made to be the Goody model.

Comparing the 1D and 2D forms of Corcos-type models across the full frequency range, it is observed that all models except for the Efimtsov model exhibit clear convective ridge characteristics. The convective ridge feature of the Efimtsov model is not prominent in the low-frequency region. In the viscous region, the FW-H-G model demonstrates higher energy magnitudes, while the other models are generally consistent. The Efimtsov model, based on the Corcos model, introduces a frequency-dependent coefficient $\Lambda_1\Lambda_3$, resulting in weaker convection ridge characteristics in the low-frequency range compared to other Corcos-type models. The Smol'yakov III model, unlike the typical approximation of convective velocity as $U_c = 0.7U_\infty$, assumes that the convective velocity U_c varies with frequency and employs its own convective velocity model. The FW-H-G model, also based on the Corcos model, incorporates a $\left(\mathbf{k}_{13}/k_c\right)^2$ term, making its amplitude dependent on the growth of the wavenumber. Overall, except for the FW-H-G model, the predictions of the other five Corcos-type models converge in the high-frequency range.

In the more theoretically driven non-Corcos type models, the MT term dominates, representing the convection ridge characteristics, while the TT term is minor and can be neglected when focusing solely on the convection ridge. The TNO and Smol'yakov II models only consider the MT term, thus both adhere to the Kraichnan-Phillips theory. In incompressible models such as Chase I, Smol'yakov II, and TNO, the solutions are derived from the Poisson equation. In compressible theoretical models, namely the Chase II and Doisy models, there is an infinite discontinuity with an infinite amplitude at the acoustic wavenumber k_0. It is worth noting that the Chase II model is based on Bergeron's assumptions of low wavenumbers and low Mach numbers, derived using a dimensionless method, while the Doisy model is based on the Lighthill equation and incorporates compressibility through the continuity equation. These two compressible models differ significantly in their fundamental modeling approaches. In comparison the non-Corcos-type models, derived from theoretical formulations, involve greater computational complexity. Among these, the Doisy and TNO models are particularly complex to compute, followed by the Smol'yakov II model. The Doisy model exhibits an overall amplitude bias, but it is anticipated to be able to be improved.

Note: all comments on the models discussed in this work are based on their original published expressions. Since then, there have been some improvements made to some of the models, but these are not the subject of the current paper.

Acknowledgments

This research was supported by National Natural Science Foundation of China with Grant No. 12261131502.

References

[1] Ren, S., Tian, B., Jones, W. P., and Wang, X., "The Response Mechanism of Pressure Fluctuation to the Unsteady Heat Release in a Strong Rotating Environment," Aerospace Science and Technology, Vol. 139, 2023, p. 108356. https://doi.org/10.1016/j.ast.2023.108356

[2] Choi, J. N., and Lee, J. H., "Active Control of Pressure Fluctuations in an Incompressible Turbulent Cavity Flow," Aerospace Science and Technology, Vol. 141, 2023, p. 108512. https://doi.org/10.1016/j.ast.2023.108512

[3] Talotte, C., Gautier, P. E., Thompson, D. J., and Hanson, C., "Identification,Modeling and Reduction Potential of Rail-wayNoise Sources: A Critical Survey," Journal of Sound and Vibration, Vol. 2, No. 267, 2003, pp. 447–468. https://doi.org/10.1016/S0022-460X%2803%2900707-7
[4] Camussi, R., Guj, G., Imperatore, B., Pizzicaroli, A., and Perigo, D., "Wall Pressure Fluctuations Induced by Transonic Boundary Layers on a Launcher Model," Aerospace Science and Technology, Vol. 11, No. 5, 2007, pp. 349–359. https://doi.org/10.1016/j.ast.2007.01.004
[5] Petrone, G., Melillo, G., Laudiero, A., and De Rosa, S., "A Statistical Energy Analysis (SEA) Model of a Fuselage Section for the Prediction of the Internal Sound Pressure Level (SPL) at Cruise Flight Conditions," Aerospace Science and Technology, Vol. 88, 2019, pp. 340–349. https://doi.org/10.1016/j.ast.2019.03.032
[6] Zhao, K., Okolo, P., Neri, E., Chen, P., Kennedy, J., and Bennett, G. J., "Noise Reduction Technologies for Aircraft Landing Gear-A Bibliographic Review," Progress in Aerospace Sciences, Vol. 112, 2020, p. 100589. https://doi.org/10.1016/j.paerosci.2019.100589
[7] Ciappi, E., De Rosa, S., Franco, F., Hambric, S. A., Leung, R. C. K., Clair, V., Maxit, L., and Totaro, N., Eds., "Flinovia—Flow Induced Noise and Vibration Issues and Aspects-III," Springer International Publishing, Cham, 2021. https://doi.org/10.1007/978-3-030-64807-7
[8] Camussi, R., Di Marco, A., Stoica, C., Bernardini, M., Stella, F., De Gregorio, F., Paglia, F., Romano, L., and Barbagallo, D., "Wind Tunnel Measurements of the Surface Pressure Fluctuations on the New VEGA-C Space Launcher," Aerospace Science and Technology, Vol. 99, 2020, p. 105772. https://doi.org/10.1016/j.ast.2020.105772
[9] Salze, E., Bailly, C., Marsden, O., Jondeau, E., and Juve, D., "An Experimental Characterisation of Wall Pressure Wavevector-Frequency Spectra in the Presence of Pressure Gradients," presented at the 20th AIAA/CEAS Aeroacoustics Conference, Atlanta, GA, 2014. https://doi.org/10.2514/6.2014-2909
[10] Schram, C. F., and Van de Wyer, N., "An Optimized Microphone Array for the Measurement of Turbulent Boundary Layer Wall Pressure Wavenumber-Frequency Spectra," presented at the 2018 AIAA/CEAS Aeroacoustics Conference, Atlanta, Georgia, 2018. https://doi.org/10.2514/6.2018-2968
[11] Manoha, E., "The Wavenumber-Frequency Spectrum of the Wall Pressure Fluctuations beneath a Turbulent Boundary Layer," presented at the Aeroacoustics Conference, State College,PA,U.S.A., 1996. https://doi.org/10.2514/6.1996-1758
[12] Corcos, G. M., "Resolution of Pressure in Turbulence," The Journal of the Acoustical Society of America, Vol. 35, No. 2, 1963, pp. 192–199. https://doi.org/10.1121/1.1918431
[13] Corcos, G. M., "The Structure of the Turbulent Pressure Field in Boundary-Layer Flows," Journal of Fluid Mechanics, Vol. 18, No. 03, 1964, p. 353. https://doi.org/10.1017/S002211206400026X
[14] Doisy, Y., "Modelling Wall Pressure Fluctuations under a Turbulent Boundary Layer," Journal of Sound and Vibration, Vol. 400, 2017, pp. 178–200. https://doi.org/10.1016/j.jsv.2017.04.004
[15] Graham, W. R., "A Comparison of Models for the Wavenumber-Frequency Spectrum of Turbulent Boundary Layer Pressures," Journal of Sound and Vibration, Vol. 206, No. 4, 1997, pp. 541–565. https://doi.org/10.1006/jsvi.1997.1114
[16] Miller, T. S., Gallman, J. M., and Moeller, M. J., "Review of Turbulent Boundary Layer Models for Acoustic Analysis," Journal of Aircraft, Vol. 49, No. 6, 2012, pp. 1739–1754. https://doi.org/10.2514/1.C031405

[17] Salze, E., Jondeau, E., Pereira, A., Prigent, S. L., and Bailly, C., “A New MEMS Microphone Array for the Wavenumber Analysis of Wall-Pressure Fluctuations: Application to the Modal Investigation of a Ducted Low-Mach Number Stage,” presented at the 25th AIAA/CEAS Aeroacoustics Conference, Delft, The Netherlands, 2019. https://doi.org/10.2514/6.2019-2574

[18] Prigent, S. L., Salze, É., Jondeau, E., and Bailly, C., “Spatial Structure and Wavenumber Filtering of Wall Pressure Fluctuations on a Full-Scale Cockpit Model,” Experiments in Fluids, Vol. 61, No. 9, 2020, p. 201. https://doi.org/10.1007/s00348-020-03017-2

[19] Blake, W. K., “Chapter 2 - Essentials of Turbulent Wall Pressure Fluctuations,” Mechanics of Flow-Induced Sound and Vibration, Volume 2 (Second Edition), edited by W. K. Blake, Academic Press, 2017, pp. 81–177. https://doi.org/10.1016/B978-0-12-809274-3.00002-7

[20] Kraichnan, R. H., “Pressure Fluctuations in Turbulent Flow over a Flat Plate,” The Journal of the Acoustical Society of America, Vol. 28, No. 3, 1956, pp. 378–390. https://doi.org/10.1121/1.1908336

[21] Bonness, W. K., Capone, D. E., and Hambric, S. A., “Low-Wavenumber Turbulent Boundary Layer Wall-Pressure Measurements from Vibration Data on a Cylinder in Pipe Flow,” Journal of Sound and Vibration, Vol. 329, No. 20, 2010, pp. 4166–4180. https://doi.org/10.1016/j.jsv.2010.04.010

[22] Chase, D. M., “Modeling the Wavevector-Frequency Spectrum of Turbulent Boundary Layer Wall Pressure,” Journal of Sound and Vibration, Vol. 70, No. 1, 1980, pp. 29–67. https://doi.org/10.1016/0022-460X(80)90553-2

[23] Efimtsov, B., “Characteristics of the Field of Turbulent Wall Pressure-Fluctuations at Large Reynolds-Numbers,” Soviet Physics Acoustics-USSR, Vol. 28, No. 4, 1982, pp. 289–292.

[24] Williams, J. E. F., “Boundary-Layer Pressures and the Corcos Model: A Development to Incorporate Low-Wavenumber Constraints,” Journal of Fluid Mechanics, Vol. 125, No. 1, 1982, p. 9. https://doi.org/10.1017/S0022112082003218

[25] Hwang, Y. F., and Geib, F. E., “Estimation of the Wavevector-Frequency Spectrum of Turbulent Boundary Layer Wall Pressure by Multiple Linear Regression,” Journal of Vibration and Acoustics, Vol. 106, No. 3, 1984, pp. 334–342. https://doi.org/10.1115/1.3269199

[26] Witting, J. M., “A Spectral Model of Pressure Fluctuations at a Rigid Wall Bounding an Incompressible Fluid, Based on Turbulent Structures in the Boundary Layer,” Noise Control Engineering Journal, Vol. 26, No. 1, 1986, p. 28. https://doi.org/10.3397/1.2827660

[27] Chase, D. M., “The Character of the Turbulent Wall Pressure Spectrum at Subconvective Wavenumbers and a Suggested Comprehensive Model,” Journal of Sound and Vibration, Vol. 112, No. 1, 1987, pp. 125–147. https://doi.org/10.1016/S0022-460X(87)80098-6

[28] Mellen, R. H., “On Modeling Convective Turbulence,” The Journal of the Acoustical Society of America, Vol. 88, No. 6, 1990, pp. 2891–2893. https://doi.org/10.1121/1.399695

[29] Mellen, R. H., “Wave-vector Filter Analysis of Turbulent Flow,” The Journal of the Acoustical Society of America, Vol. 95, No. 3, 1994, pp. 1671–1673. https://doi.org/10.1121/1.408556

[30] Smol’Yakov, A., Tkachenko, V., and Wood, J., “Model of a Field of Pseudosonic Turbulent Wall Pressures and Experimental Data,” Soviet physics. Acoustics, Vol. 37, No. 6, 1991, pp. 627–631.

[31] Parchen, R., “Progress Report DRAW: A Prediction Scheme for Trailing Edge Noise Based on Detailed Boundary Layer Characteristics,” HAG-RPT-980023, TNO Institute of Applied Physics, January 1998.

[32] Moriarty, P., Guidati, G., and Migliore, P., "Prediction of Turbulent Inflow and Trailing-Edge Noise for Wind Turbines," presented at the 11th AIAA/CEAS Aeroacoustics Conference, Monterey, California, 2005. https://doi.org/10.2514/6.2005-2881

[33] Smol'yakov, A. V., "Calculation of the Spectra of Pseudosound Wall-Pressure Fluctuations in Turbulent Boundary Layers," Acoustical Physics, Vol. 46, No. 3, 2000, pp. 342–347. https://doi.org/10.1134/1.29890

[34] Smol'yakov, A. V., "A New Model for the Cross Spectrum and Wavenumber-Frequency Spectrum of Turbulent Pressure Fluctuations in a Boundary Layer," Acoustical Physics, Vol. 52, No. 3, 2006, pp. 331–337. https://doi.org/10.1134/S1063771006030146

[35] Cheng, J., and Miller, S. A. E., "The Prediction of Cross-Spectra from First Mode Instability Waves within High-Speed Flow over Sharp and Blunt Cones with Plasma Actuation," Aerospace Science and Technology, Vol. 130, 2022, p. 107870. https://doi.org/10.1016/j.ast.2022.107870

[36] Corcos, G. M., "The Resolution of Turbulent Pressures at the Wall of a Boundary Layer," Journal of Sound and Vibration, Vol. 6, No. 1, 1967, pp. 59–70. https://doi.org/10.1016/0022-460X(67)90158-7

[37] Bull, M. K., "Wall-Pressure Fluctuations Associated with Subsonic Turbulent Boundary Layer Flow," Journal of Fluid Mechanics, Vol. 28, No. 4, 1967, pp. 719–754. https://doi.org/10.1017/S0022112067002411

[38] Chase, D. M., "Recent Modeling of Turbulent Wall Pressure and Fluid Interaction With a Compliant Boundary," Journal of Vibration and Acoustics, Vol. 106, No. 3, 1984, pp. 328–333. https://doi.org/10.1115/1.3269198

[39] Kraichnan, R. H., "Pressure Field within Homogeneous Anisotropic Turbulence," The Journal of the Acoustical Society of America, Vol. 28, No. 1, 1956, pp. 64–72. https://doi.org/10.1121/1.1908224

[40] Lighthill, M. J., "On Sound Generated Aerodynamically. I. General Theory," Proceedings of the Royal Society of London. Series A, Mathematical and Physical Sciences, Vol. 211, No. 1107, 1952, pp. 564–587. https://doi.org/10.2307/98943

[41] Williams, J. E. F., "Surface-Pressure Fluctuations Induced by Boundary-Layer Flow at Finite Mach Number," Journal of Fluid Mechanics, Vol. 22, No. 3, 1965, pp. 507–519. https://doi.org/10.1017/S0022112065000939

[42] Witting, J. M., "A Spectral Model of Pressure Fluctuations at a Rigid Wall Bounding an Incompressible Fluid, Based on Turbulent Structures in the Boundary Layer," Noise Control Engineering Journal, Vol. 26, No. 1, 1986, p. 28. https://doi.org/10.3397/1.2827660

[43] Kline, S. J., Reynolds, W. C., Schraub, F. A., and Runstadler, P. W., "The Structure of Turbulent Boundary Layers," Journal of Fluid Mechanics, Vol. 30, No. 4, 1967, pp. 741–773. https://doi.org/10.1017/S0022112067001740

[44] Robinson, S. K., "Coherent Motions in the Turbulent Boundary Layer," Annual Review of Fluid Mechanics, Vol. 23, No. 1, 1991, pp. 601–639. https://doi.org/10.1146/annurev.fl.23.010191.003125

[45] Bergeron, R. F., "Aerodynamic Sound and the Low-wavenumber Wall-pressure Spectrum of Nearly Incompressible Boundary-layer Turbulence," The Journal of the Acoustical Society of America, Vol. 54, No. 1, 1973, pp. 123–133. https://doi.org/10.1121/1.1913553

[46] Chase, D. M., and Noiseux, C. F., "Turbulent Wall Pressure at Low Wavenumbers: Relation to Nonlinear Sources in Planar and Cylindrical Flow," The Journal of the Acoustical Society of America, Vol. 72, No. 3, 1982, pp. 975–982. https://doi.org/10.1121/1.388179

[47] Chase, D. M., “Recent Modeling of Turbulent Wall Pressure and Fluid Interaction With a Compliant Boundary,” Journal of Vibration and Acoustics, Vol. 106, No. 3, 1984, pp. 328–333. https://doi.org/10.1115/1.3269198

[48] Lutz, T., Herrig, A., Würz, W., Kamruzzaman, M., and Krämer, E., “Design and Wind-Tunnel Verification of Low-Noise Airfoils for Wind Turbines,” AIAA Journal, Vol. 45, No. 4, 2007, pp. 779–785. https://doi.org/10.2514/1.27658

[49] Bertagnolio, F., Fischer, A., and Jun Zhu, W., “Tuning of Turbulent Boundary Layer Anisotropy for Improved Surface Pressure and Trailing-Edge Noise Modeling,” Journal of Sound and Vibration, Vol. 333, No. 3, 2014, pp. 991–1010. https://doi.org/10.1016/j.jsv.2013.10.008

[50] Stalnov, O., Chaitanya, P., and Joseph, P. F., “Towards a Non-Empirical Trailing Edge Noise Prediction Model,” Journal of Sound and Vibration, Vol. 372, 2016, pp. 50–68. https://doi.org/10.1016/j.jsv.2015.10.011

[51] Kamruzzaman, M., Lutz, Th., Würz, W., Shen, W. Z., Zhu, W. J., Hansen, M. O. L., Bertagnolio, F., and Madsen, H. Aa., “Validations and Improvements of Airfoil Trailing-Edge Noise Prediction Models Using Detailed Experimental Data: Validations and Improvements of Aeroacoustic Models,” Wind Energy, Vol. 15, No. 1, 2012, pp. 45–61. https://doi.org/10.1002/we.505

[52] Coles, D., “The Law of the Wake in the Turbulent Boundary Layer,” Journal of Fluid Mechanics, Vol. 1, No. 2, 1956, pp. 191–226. https://doi.org/10.1017/S0022112056000135

[53] Fischer, A., Bertagnolio, F., and Madsen, H. Aa., “Improvement of TNO Type Trailing Edge Noise Models,” European Journal of Mechanics - B/Fluids, Vol. 61, 2017, pp. 255–262. https://doi.org/10.1016/j.euromechflu.2016.09.005

[54] Dowling, A. P., “Mean Flow Effects on the Low-Wavenumber Pressure Spectrum on a Flexible Surface,” Journal of Fluids Engineering, Vol. 108, No. 1, 1986, pp. 104–108. https://doi.org/10.1115/1.3242527

[55] Pope, S. B., “Turbulent Flows,” Cambridge University Press, 2000.

[56] Abraham, B. M., and Keith, W. L., “Direct Measurements of Turbulent Boundary Layer Wall Pressure Wavenumber-Frequency Spectra,” Journal of Fluids Engineering, Vol. 120, No. 1, 1998, pp. 29–39. https://doi.org/10.1115/1.2819657

[57] Goody, M., “Empirical Spectral Model of Surface Pressure Fluctuations,” AIAA Journal, Vol. 42, No. 9, 2004, pp. 1788–1794. https://doi.org/10.2514/1.9433

Appendix A

The most commonly used mathematical definition for Fourier transformation is:

$$\begin{cases} F(\omega) = \int_{-\infty}^{\infty} f(t) e^{-i\omega t} dt \\ f(t) = \dfrac{1}{2\pi} \int_{-\infty}^{\infty} F(\omega) e^{i\omega t} d\omega \end{cases} \tag{A.1}$$

, here $F(\omega)$ and $f(t)$ represent the transformation and the inverse transformation, respectively. However, in some areas, alternative mathematical definitions may be applied, namely:

$$\begin{cases} F(\omega) = \dfrac{1}{2\pi} \int_{-\infty}^{\infty} f(t) e^{i\omega\Delta t} dt \\ f(t) = \int_{-\infty}^{\infty} F(\omega) e^{-i\omega\Delta t} d\omega \end{cases} \tag{A.2}$$

or:

$$\begin{cases} F(\omega) = \dfrac{1}{2\pi} \int_{-\infty}^{\infty} f(t) e^{-i\omega t} dt \\ f(t) = \int_{-\infty}^{\infty} F(\omega) e^{i\omega t} d\omega \end{cases} \tag{A.3}$$

The difference lies in whether there is a $1/(2\pi)$ and whether there is a positive or negative sign in the natural logarithm exponent. Whether there is a $1/(2\pi)$ will affect the results in terms of the amplitude; however, whether there is a positive or negative sign in the natural logarithm exponent do not affect the mathematical and physical properties of the Fourier transform. In the study presented in this paper, the form (A.3) is employed.